Journal of the Meteorological Society of Japan

EARLY ONLINE RELEASE

The DOI for this manuscript is
DOI:10.2151/jmsj.2020-062
J-STAGE Advance published date: August 12th 2020
The final manuscript after publication will replace the preliminary version at the above DOI once it is available.

Characteristics of Large-Scale Atmospheric Fields during Heavy Rainfall Events in Western Japan: Comparison with an Extreme Event in Early July 2018

Yayoi HARADA[1], Hirokazu ENDO

Meteorological Research Institute, Tsukuba, Japan

and

Kazuto TAKEMURA

Climate Prediction Division, Japan Meteorological Agency, Tokyo, Japan
Graduate School of Science, Kyoto University, Kyoto, Japan

February 21, 2020

----
1) Corresponding author: Yayoi Harada, Meteorological Research Institute, 1-1, Nagamine, Tsukuba, Ibaraki 305-0052 JAPAN.
Email: yharada@mri-jma.go.jp

Abstract

To explore large-scale atmospheric factors causing heavy rainfall events that occurred widely in western Japan, a composite analysis of atmospheric fields during the past heavy rainfall events in the region is performed using the Japanese 55-year Reanalysis. During heavy rainfall events, atmospheric fields are characterized by an upper-tropospheric trough over the Korean Peninsula (KP), an upper-tropospheric ridge to the east of Japan, a surface high-pressure system to the southeast of Japan, and southwesterly moisture flux. The composite analysis indicates that a clear wave train due to quasi-stationary Rossby wave-packet propagation (RWPP) along the polar front jet (PFJ) over Siberia tends to occur just before extreme events. Further analysis considering various time-scale variabilities in the atmosphere reveals that surface high-pressure anomalies to the southeast of Japan are dominated by variability with a 25–90-day period, whereas variability with an 8–25-day period dominates lower-pressure anomalies over the East China Sea (ECS) in relation to the development of the upper-tropospheric trough around the KP.

We also investigate atmospheric fields during an extreme heavy rainfall event that occurred in early July 2018 (HR18). Atmospheric features during HR18 are generally similar to those of the other heavy rainfall events. However, a remarkable RWPP occurred along the sub-tropical jet (STJ) in late June 2018 and intensified a surface high-pressure system to the southeast of Japan. In addition, a low-pressure system with an 8–25-day period to the south of Japan developed in association with wave breaking induced by the remarkable RWPP along the STJ and propagated northwestward toward the ECS and then to Japan. The simultaneous development of high- and low-pressure systems contributed to the extreme southerly moisture flux into western Japan. HR18 is also characterized by a sharp upper-tropospheric trough over the KP that is dominated by high-frequency variability with a period <8 days.

Keywords heavy rainfall; Rossby wave packet propagation; wave breaking; water vapor flux

1. Introduction

Heavy rainfall events often occur during the rainy summer monsoon season in Japan, known as the Baiu. Such events occasionally cause flooding and have serious socio-economic impacts. For example, in early July 2018 an extreme heavy rainfall event, we refer to this event as HR18 (Heavy Rainfall event in 2018), occurred and seriously impacted western Japan and the adjacent Tokai region, located to the east of western Japan (Tsuguti et al. 2018; Shimpo et al. 2019). Takemura et al. (2019) revealed that both a shallow southerly airstream caused by the surface North Pacific Subtropical High and a deeper southwesterly airstream due to enhanced convection over the East China Sea (ECS) contributed to the extensive rainfall. Yokoyama et al. (2020) performed a detailed analysis of the atmospheric fields around Japan and identified the importance of an upper-tropospheric trough which stayed to the rear of the extensive rainfall area, and also discussed the cause of this extreme event in terms of both dynamical and diabatic effects.

Akiyama (1975) identified the important contribution of moisture flux from the subtropical Pacific to extreme heavy rainfalls. Several case studies have focused on heavy rainfall events in Japan (e.g., Ninomiya 1978; Akiyama 1984, 1989; Kato and Goda 2001; Shibagaki and Ninomiya 2005). Ninomiya and Akiyama (1992) argued the importance of the interaction between the multi-scale (e.g., planetary, synoptic, and mesoscale) phenomena in the occurrence of heavy rainfall. Ninomiya (2001) and Ninomiya and Shibagaki (2007) performed ***Q***-vector analyses of observational data and found a role for the upper-tropospheric trough in the intense rainfall of July 1991.

Yoshida and Ito (2012) examined, using a case study, the indirect effect of tropical cyclones on heavy rainfall during the Baiu season in Kyushu, and discussed a contribution by a large moisture flux oriented toward the south of Kyushu. Hirota et al. (2016) examined factors causing an extreme rainfall event that occurred in Hiroshima, Japan on 9 August 2014, and found considerable filamentary transport of water vapor from the Indochina Peninsula to the Japanese islands. They also pointed out the importance of a cut off low detached from the subtropical jet (STJ) over the central Pacific. Kamae et al. (2017) evaluated the contribution of atmospheric rivers (low-level moisture flows) to the hydrological cycle over East Asia, and identified a relationship between heavy rainfall in the warm season and the El Niño of the preceding winter.

Furthermore, Kosaka et al. (2011) showed the statistical relationship between a 30-day Meiyu–Baiu precipitation in early summer and the El Niño–Southern Oscillation in preceding boreal winter, Pacific–Japan teleconnection (Nitta 1987), Silk Road pattern along the Asian jet (Enomoto et al. 2003), a wave train pattern along the polar front jet (PFJ). They also discussed the role of the Pacific–Japan teleconnection pattern as a medium between the El Niño–Southern Oscillation and Meiyu–Baiu precipitation. Hirota and Takahashi (2012) argued the importance of both southward upper-tropospheric and northward lower-tropospheric Rossby wave propagations in the formation of a tri-polar anomaly pattern with centers located around the Philippines, China/Japan, and East

Siberia which dominantly appears in climate variations of the East Asian summer monsoon and is closely related to the inter-annual variations of the Baiu. However, the relationships between heavy rainfall events over western Japan in the warm season and large-scale variability, such as quasi-stationary Rossby wave packet propagation (RWPP), over Eurasia have not been clarified.

This study examines statistical large-scale atmospheric characteristics during the past heavy rainfall events, which have occurred widely in western Japan since 1979, using the Japanese 55-year Reanalysis including near-real-time data (JRA-55; Kobayashi et al. 2015). We also compare these characteristics during previous heavy rainfall events with those during HR18. This type of investigation can help clarify the large-scale atmospheric factors that cause heavy rainfall events in western Japan. A comprehensive understanding of these factors will be useful for early warning systems and for the mitigation of adverse socio-economic effects, as these events continue to occur frequently in western Japan.

The reminder of this paper is organized as follows. Section 2 describes the data and analysis methods. Results of the composite analysis of historical events and a comparison with HR18 are provided in section 3. Section 4 discusses a possible mechanism that explains the atmospheric characteristics during HR18. Finally, a summary and conclusions are given in section 5.

2. Data and methods

2.1 Data

In this study, we use *in-situ* observational precipitation derived from the Japan Meteorological Agency (JMA) Automated Meteorological Data Acquisition System (AMeDAS) to extract past heavy rainfall events that occurred widely in western Japan. To analyze the atmospheric fields, we use surface, isobaric, total-column, and isentropic analysis fields from JRA-55 products with a horizontal resolution of 1.25º in both latitude and longitude. National Oceanic and Atmospheric Administration (NOAA) Interpolated Outgoing Longwave Radiation (OLR) data (Liebmann and Smith 1996) are also used. We utilize the daily-climatology defined as averages for the period 1981–2010, which is according to a definition by Japan Meteorological Agency, and filtered by 60-day low-pass filter (LPF) based on Duchon (1979). The details of this filter are described in Section 2.2. We define anomalies as deviations from the climatology.

2.2 Methods

To extract past heavy rainfall events from the historical data, we average AMeDAS daily precipitation over western Japan, using data from the 296 AMeDAS stations that are continuously available for the 40 years from 1979 to 2018, and area-averaged daily-total precipitation are accumulated over a 3-day period centered around each day during the warm season (from May to September) for the study period. We then identify heavy rainfall events as 3-day precipitation that exceeds the 95th percentile (Fig. 1). Note that if two extracted dates are <8 days apart, we consider them to be the same event, with the date of the event corresponding to the peak 3-day precipitation during the event. We exclude events when a typhoon center exists within 500 km from the measurement stations used in the analysis (gray bars in Fig. 1, 35 events) to avoid confusion between the direct effects of typhoons related to landfall and other atmospheric processes (Kamahori 2012). The total number of heavy rainfall events identified in this study is 42. We exclude HR18 from the composite analysis (red bar in Fig. 1). For the composite analysis, we extract 30 events from the heavy rainfall events described above and classify them into three groups by total precipitation: the highest 10 (TP10), middle 10 (MD10), and lowest 10 (LW10) events, which are represented by orange bars, yellow bars, and green bars in Fig. 1, respectively. Statistical significance is calculated using Student's *t*-test. The 90% and 95% confidence levels are used to indicate statistical significance.

In this study, we diagnose the quasi-stationary RWPP using the wave activity flux (WAF) given by Takaya and Nakamura (2001). They derived an approximate conservation relation of the wave-activity pseudo-momentum for quasi-geostrophic eddies on a zonally varying basic flow by averaging neither in time nor in space. The horizontal component of WAF is defined as follows:

$$\mathbf{W} = \frac{p\,cos\emptyset}{2|\mathbf{U}|}\begin{pmatrix} \frac{U}{a^2cos^2\emptyset}\left[\left(\frac{\partial\psi'}{\partial\lambda}\right)^2 - \psi'\frac{\partial^2\psi'}{\partial\lambda^2}\right] + \frac{V}{a^2cos\emptyset}\left[\frac{\partial\psi'}{\partial\lambda}\frac{\partial\psi'}{\partial\emptyset} - \psi'\frac{\partial^2\psi'}{\partial\lambda\partial\emptyset}\right] \\ \frac{U}{a^2cos\emptyset}\left[\frac{\partial\psi'}{\partial\lambda}\frac{\partial\psi'}{\partial\emptyset} - \psi'\frac{\partial^2\psi'}{\partial\lambda\partial\emptyset}\right] + \frac{V}{a^2}\left[\left(\frac{\partial\psi'}{\partial\emptyset}\right)^2 - \psi'\frac{\partial^2\psi'}{\partial\emptyset^2}\right] \end{pmatrix} + \boldsymbol{C}_u M, \quad (1)$$

where $\mathbf{U}$=(U, V) is a steady zonally varying basic flow defined as the climatological horizontal winds, p is pressure normalized by 1000 hPa, and $\emptyset$ and λ are latitude and longitude, respectively. A prime denotes the anomalies. The stream-function and radius of the Earth are noted by ψ and a, respectively. Since the rightmost term "$\boldsymbol{C_u M}$" represents effect of the phase propagation and this study are focusing on the quasi-stationary Rossby wave, we consider that this term can be ignored. The WAFs are derived from 3-day mean fields.

To assess the contributions of atmospheric variability over various timescales to the occurrence of rainfall events, we apply a Lanczos filter (Duchon 1979) to the JRA-55 products. This digital filtering involves transforming an input data sequence x_t, where t is time, into an output data sequence y_t using the linear relationship

$$y_t = a_0 + \sum_{n=1}^{\infty} w_k x_{t-k}, \tag{2}$$

in which w_k are suitably chosen weights. For example, weights for a high-pass filter (HPF) are calculated as follows:

$$w_k = \frac{\sin(2\pi f_c k)}{\pi k} \frac{\sin(\pi k/n)}{\pi k/n}, k = -n, \cdots, 0, \cdots, n, \tag{3}$$

where fc and $2n+1$ are the cutoff frequency and sample size for filtering, respectively. Weights for a LPF can be obtained by subtracting those for a HPF from one. We can obtain weights for a band-pass filter (BPF) using weights for two LPFs with different cutoff frequencies. In this study, an 8-day HPF, an 8–25-day BPF, a 25–90-day BPF, a 90-day LPF, and a 25-day LPF are utilized. Synoptic-scale eddies have 8-day or shorter periods, and the 25-90-day period corresponds to intra-seasonal variability such as the Madden-Julian Oscillation in the previous studies (e.g., Kikuchi et al. 2012). In addition, 8-25-day BPF extracts intermediate variability between Synoptic-scale eddies and intra-seasonal variability.

3. Results

3.1 Composite analysis of 3-day mean fields and comparison with HR18

Table 1 lists the dates and 3-day precipitation averaged over western Japan for the top 21 heavy rainfall events. The dates in Table 1 represent the central dates for the 3-day accumulated precipitation. It is noteworthy that the precipitation during HR18 exceeds 250 mm, and represents the largest value among the events. Most events affected by the landfall or passage of a typhoon occurred in September (Table 1). Most other events, in contrast, occurred in June or July, during the Baiu. The highest-precipitation non-typhoon events, which rank from 3rd (205.9 mm) to 21st (139.2 mm) of the total events by precipitation, are used for the composite analysis as “TP10”. As shown in Fig. 1, 3-day precipitation for events MD10 and LW10 are 100 to 125 mm and 75 to 100 mm, respectively. The results of the composite analysis for these events are also assessed in this study.

Figure 2 shows composite atmospheric fields around Japan for TP10. In the upper troposphere, positive vorticity anomalies over the Korean Peninsula (KP) and a wide area of negative vorticity anomalies centered over Japan are statistically significant (Fig. 2a), and significant westerly wind anomalies are distributed along the large gradient of the vorticity anomalies (Fig. 2b). At 500-hPa geopotential height (Fig. 2d), significant negative height anomalies over the KP and positive height anomalies to the east of Japan are also evident. These features represent the development of the upper-tropospheric trough over the KP and the upper tropospheric ridge to the east of Japan, contributing to a dynamically induced mid-level ascent ahead of the trough from China to Japan, where upwelling anomalies are statistically significant at 500 hPa (Fig. 2c). Note that these upwelling anomalies also include diabatic forcing by active convection (Fig. 2h). In the lower troposphere, horizontal distribution of significant positive vorticity anomalies is generally consistent with that of significant mid-level upwelling anomalies from China to Japan (Fig. 2e). Sea level pressure (SLP; Fig. 2f) exhibits statistically significant high-pressure anomalies to the southeast of Japan, which indicate the development and persistence of a high-pressure system in the area. Low-pressure anomalies to the west of Kyushu are also statistically significant. Vertically integrated moisture flux (Fig. 2g) indicates an anomalous southwesterly moisture inflow toward Japan along the western-to-northern fringe of the high-pressure anomalies (Fig. 2f). Statistically significant moisture flux convergence (contours in Fig. 2g) is analyzed immediately over the region of the upwelling anomalies at 500 hPa (Fig. 2c). These features in the composite maps indicate that the surface high-pressure system to the southeast of Japan plays an important role in moisture transport during heavy rainfall events, consistent with the results of Akiyama (1975).

As described above, TP10 is characterized by an upper-tropospheric deepened trough over the KP, an upper-tropospheric ridge to the east of Japan, a surface high-pressure system to the southeast of Japan, and southwesterly moisture flux in the lower troposphere. These features are also present but weaker for MD10 and LW10 (not shown).

Figures 3 and 4 show the upper-tropospheric RWPPs preceding heavy rainfall events for TP10, and for MD10 and LW10, respectively. Comparing the three groups, TP10 experiences persistent wave train along the PFJ (Figs. 3a-d). The existence of the wave packet propagation along the PFJ in summertime is consistent with related previous studies (e.g., Iwao and Takahashi 2008; Nakamura and Fukamachi 2004; Ogasawara and Kawamura 2008). The wave packets in TP10 propagate from northern Europe to eastern Siberia along the PFJ (Figs. 3a–c), and contribute to the enhancement of the ridge to the east of Japan (Fig. 3d). In contrast, the wave packets propagating along the STJ over central Asia (Fig. 3b) contribute to the enhancement of the trough over the KP and, in turn, the ridge to the east of Japan (Fig. 3d), although this wave train is not as clear as that along the PFJ. During MD10 (Figs. 4a–d), the wave packets emanating from western Europe propagate along the STJ and strengthen the trough over the KP and the ridge to the east of Japan (Fig. 4d). Although RWPPs are clearly seen over Eurasia before LW10 (Figs. 4e–g), their contribution to the enhancement of the anomalous circulation around Japan is unclear during LW10 (Fig. 4h). These results indicate that RWPPs over Eurasia, particularly along the PFJ, play an important role in extreme heavy rainfall events such as TP10.

Next, anomalous atmospheric fields for HR18 (Fig. 5) are compared with those of TP10 (Fig. 2). In the upper troposphere (Fig. 5a), the trough over the KP is sharper compared with that of TP10 (Fig. 2a). Dynamical forcing by the trough over the KP plays an important role in inducing strong upwelling over western Japan, as indicated by Yokoyama et al. (2020) and Takemura et al. (2019), although the trough is not obvious in the 500-hPa height anomaly field (Fig. 5d). This is partly associated with significantly warm conditions at mid-latitudes, as suggested by Kobayashi and Ishikawa (2019) and Takemura et al. (2019). In the mid-troposphere, strong upwelling anomalies are concentrated over western Japan (Fig. 5c), and lower-tropospheric positive vorticity anomalies are distributed from the ECS to western Japan (Fig. 5e). This differs from the conditions of TP10 events, particularly over the ECS (Fig. 2e). The SLP shown in Fig. 5f indicates that high-pressure anomalies to the southeast of Japan are comparable to those of TP10 (Fig. 2f), and low-pressure anomalies over the ECS are stronger than those of TP10. Consequently, southerly moisture flux is concentrated in the region 130°–135°E to the south of western Japan (Fig. 5g). These features indicate that both the high-pressure system to the southeast of Japan and the low-pressure system over the ECS contribute to the enhanced southerly moisture flow toward western Japan, as indicated by Takemura et al. (2019). Although the high-pressure system to the southeast of Japan is not extremely strong (Fig. 6a) and the low-pressure system over the ECS is not significant compared with other historical events (not shown), their simultaneous occurrence contributes to the intensification of the southerly flow toward western Japan in the lower troposphere. The regionally averaged meridional wind at 925 hPa during HR18 (Fig. 6b) represents the third-strongest southerly flow toward western Japan among the analyzed events, and is associated with an enhanced pressure gradient in the region. In addition, specific humidity in the region shows positive anomaly, although it is not extreme value at all (Fig. 6c). The lower-tropospheric southerly moisture flux in the region is the strongest among the analyzed events (Fig. 6d), and the consequent convergence of vertically integrated moisture flux over western Japan is greatest among the events (Fig. 6e). These enhanced moisture flux and its convergence, which are strongest compared with TP10, are consistent with the anomalous meridional wind and specific humidity in the lower troposphere. For all the analyzed events, the moisture flux convergence due to wind anomalies at 925 hPa are more correlated with precipitation over western Japan than are wind anomalies at higher levels (Fig. S1). Therefore, the simultaneous occurrence of the high-pressure system to the southeast of Japan and the low-pressure system over the ECS is one of the most important characteristics of HR18. In addition, it should be noted that the moisture flux convergence due to specific humidity anomaly at 700 hPa for HR18 is extremely large compared to those for the other rainfall events (Fig. S1c). This is consistent with the result of Yokoyama et al. (2020), who conducted a detailed analysis of the atmospheric field around Japan. They showed that the moistening in the mid-troposphere was caused by the dynamical forced ascent associated with the upper-tropospheric trough which lingered in the region from the KP to the Sea of

Japan. They also pointed out the importance of the moistening in the mid-troposphere in further development of deep cumulus convection and its organization.

Figure 7 shows the upper-tropospheric RWPP from Eurasia to Japan during HR18. In late June (Figs. 7a and 7b), a remarkable RWPP—the strongest among the analyzed events (Fig. S2)—occurs along the STJ and strengthens the upper-tropospheric ridge to the east of Japan. This enhanced ridge causes the subsequent formation of a surface high pressure system to the southeast of Japan (Fig. 5f), corresponding to a formation mechanism of the Bonin high with the equivalent barotropic structure (Enomoto et al. 2003). The ridge to the east of Japan once weakens at the beginning of July (Fig. 7c), but strengthens again because of the subsequent RWPP along the PFJ accompanied by an amplified wave train (Fig. 7d). The features of the RWPP along the PFJ during HR18 are generally consistent with those of TP10, although the phases of their wave trains differ. We will discuss another role of the strong RWPP along the STJ just before HR18 in section 4.

3.2 Analysis of atmospheric variability at various time scales

In this section, we analyze detailed circulation features, using several time filters.

Figures 8 a-d (left panels) show composite maps of time-filtered SLP anomalies for TP10. High-pressure anomalies to the southeast of Japan are evident and statistically significant in this region with all-time filters except the 8-day HPF. With the 25–90-day BPF, which corresponds to the intra-seasonal time scale, these anomalies are particularly evident (Fig.

8c). It is noteworthy that the 25–90-day BPF anomalies of MD10 and LW10 are weaker than those of TP10 (see also Fig. S3). During HR18 (Figs. 8e-h), fluctuations with 25–90-day periods are strong, and are associated with the development of the high-pressure system to the southeast of Japan (Fig. 8g). In the upper troposphere, intra-seasonal time-scale variability is evident for TP10 and HR18, and is accompanied by a wave train from northern Eurasia to Japan (Fig. 9), which contributes to the enhancement of the anomalous anticyclone to the east of Japan. These results indicate the importance of RWPPs along the PFJ to anomalous circulation around Japan, including surface high-pressure systems to the southeast of Japan. Convective activity around the Philippines is also expected to contribute to the development of surface high-pressure systems to the southeast of Japan (Nitta 1987; Kosaka and Nakmura 2010). The composite map of OLR anomalies filtered using the 25–90-day BPF reveals enhanced convective activity around the Philippines, which is associated with a northward migration of the Boreal summer inter-seasonal oscillation (BSISO; Fig. 9g; see also Fig. S4). Such convective activity is not evident using the 8-day HPF, the 8–25-day BPF, or the 90-day LPF (Figs. 9e, f, and h). However, during HR18 (Fig. 9o), enhanced convective activity associated with the BSISO is located to the south of the Philippines, which is far from the surface high-pressure system to the southeast of Japan. It is therefore likely that the direct contribution of convective activity around the Philippines to the development of the surface high-pressure system to the southeast of Japan during HR18 is smaller than for TP10.

Next, we focus on surface low-pressure anomalies from the ECS to Japan filtered using the 8–25-day BPF (Fig. 8f). In the composite analysis for TP10, they are statistically significant (Fig. 8c) which are related to the development of the upper-tropospheric trough around the KP (Fig. 9b). The development of the upper-tropospheric trough is also seen during HR18 (Fig. 9j), however, it is centered over the Sea of Japan and shifts north-eastward compared to that in TP10. On the other hand, surface low-pressure anomalies over the ECS during HR18 are clearer than those of TP10 (compare Figs. 8f and 8c). This feature can not be explained by the development of the upper-tropospheric trough only. Takemura et al. (2019) pointed out the importance of lower-tropospheric cyclonic circulation anomalies over the ECS to the southerly moisture flux toward western Japan using a potential vorticity (PV) budget analysis of HR18, and argued that diabatic heating associated with active convection over the ECS acts to maintain lower-tropospheric cyclonic circulation anomalies. In this study, we investigate the time-evolution of surface low-pressure anomalies over the ECS from late June to early July 2018 (Fig. 10). On 26 June 2018 (Fig. 10a), negative OLR anomalies at 20°N, 140°E are observed and are associated with enhanced convection in this region and weak low-pressure anomalies in the western part of the region. Both the active convection and the low-pressure anomalies intensify and propagate northwestward toward the ECS until the beginning of July 2018 (Figs. 10b–d), before moving into Japan in early July (Figs. 10e and 10f). Although the low-pressure anomalies partly correspond to the track of typhoon Prapiroon, which rapidly moved northward to the north of western Japan on 4 July (not shown), the enhanced convection and low-pressure anomalies persisted over the ECS in early July. Enomoto (2019) showed, using a forecast experiment, the role of Prapiroon in the intensification of the Baiu frontal zone during HR18. We argue that the persistence of the low-pressure system over the ECS also played an important role in maintaining the lower-tropospheric southerly moisture flux during HR18. These results indicate that the development of active convection at 20°N, 140°E in late June 2018 is closely related to both the persistence of the low-pressure system over the ECS and the formation of typhoon Parpiroon. A possible mechanism for the development of this active convection is discussed in section 4.

Next, we focus on the upper-tropospheric trough over the KP during HR18, which is much sharper than that of TP10. Composite maps of the time-filtered 360-K PV anomalies (left panels of Fig. 11) indicate that the contribution of lower-frequency variability to the development of the trough over the KP is larger than that of higher-frequency variability. The amplitude of the positive PV anomalies filtered using the 25-day LPF (~1.25 PVU) is ~1.5 times larger than those filtered using the 8–25-day BPF. However, positive PV anomalies filtered using the 25-day LPF is not evident over the KP during HR18 (right panels of Fig. 11), which indicates the importance of variabilities with periods shorter than 25 days. In particular, during HR18, positive PV anomalies filtered using the 8-day HPF are much larger than those of TP10 (compare Figs. 11a and 11d). Comparing the maximum positive PV anomalies over the KP during HR18 with those of the other heavy rainfall events over western Japan that exceed the 95th percentile (Fig. 12), it is clear that PV anomalies filtered using the 8-day HPF over the KP during HR18 are particularly high. This result indicates that the predominance of higher frequency variability caused the development of the sharp upper-tropospheric trough over the KP associated with the concentration of strong mid-tropospheric upwelling anomalies over western Japan during HR18. This is discussed further in section 4.

4. Discussion

4.1 Additional effects of the strong RWPP along the STJ during June 2018

We have shown that the remarkable RWPP observed in late June 2018 strengthened the upper-tropospheric ridge to the east of Japan and consequently intensified the surface high-pressure system to the southeast of Japan. We discuss additional effects of this strong RWPP in this section. The strong RWPP along the STJ caused a wave breaking around the Date Line and the consequential evident penetration of positive PV anomalies toward the sub-tropical region to the south of Japan (Fig. 13a). These positive PV anomalies were accompanied by negative potential temperature anomalies at the dynamical tropopause (Fig. 13b). Vertical and longitudinal distribution of the square of Brunt-Vaisälä frequency anomaly shown in Figs. 13c and 13d indicate that the upper-tropospheric cold temperature leads to thermodynamically unstable atmospheric conditions and activates convection around 20°N, 140°E (Fig. 13e), which propagated from the east. Although we calculate the divergence of 500-hPa ***Q***-vectors over this region to examine if dynamically induced ascent due to positive PV intrusion exists, a clear convergence of the ***Q***-vectors is not found over the activated convection (not shown). These results indicate that thermodynamic instability made the primary contribution to the further development of convective activity around 20°N, 140°E during HR18. As discussed in section 3.2, active convection propagated northwestward toward the ECS during HR18, and was accompanied by a surface low-pressure system that remained over the ECS and played an important role in the persistent southwesterly moisture flux in the lower troposphere. The remarkable RWPP along the STJ in late June is thus one of the essential factors for the occurrence of HR18.

4.2 Possible mechanism for the formation of a sharp upper-tropospheric trough over the KP

In section 3.2, we found that PV anomalies filtered using a 8-day HPF over the KP during HR18, which are much larger than those of TP10, contributed to the development of a sharp upper-tropospheric trough over the KP. In this section, we describe the development of this upper-tropospheric trough over the KP and discuss a possible mechanism for the higher frequency variability in this region.

Figure 14 shows the time-evolution of 360-K PV anomalies around Japan from 12 UTC 5 to 06 UTC 7 July 2018. At 12 UTC 5 July (Fig. 14a), southward penetration of positive PV anomalies toward KP is found in association with weak RWPP along the STJ (see also Fig. 7d). The longitudinal horizontal scale of the positive PV anomalies gradually decreases over KP from 12 UTC 5 July to 06 UTC 7 July (Figs. 7b–d). In other words, positive PV anomalies are stagnant over the KP, on the other hand, low PV anomalies over northern China gradually move eastward. Regarding the 90-day LPF 200-hPa zonal wind field as a basic flow (Fig. 15a), the STJ is located over northern China and is accompanied by regional maximum zonal winds >30 m s^{-1} from 80°E to 100°E and slower winds (<20 m s^{-1}) in the region 100°E to 120°E. The zonal winds are even weaker over the KP. Thus, the region from northern China to the KP can be considered as one of the exit regions of the STJ, where Rossby waves tend to be stagnant and amplified (Shutts 1983; Nakamura and Huang 2017). Therefore, we compare the longitudinal gradient of 90-day LPF 200-hPa zonal winds in the region among the heavy rainfall events over western Japan (Fig. 15b). We find that the deceleration of zonal wind during HR18 is larger around 115°E than it is during other events. These results indicate that the basic flow in the STJ exit region during HR18 leads to the stagnation and amplification of Rossby waves. As discussed in section 3.1, during summer 2018, the seasonal-mean upper-tropospheric geopotential height anomalies are positive in the mid-latitudes of the Northern Hemisphere, particularly over northern China in association with the several extreme heat events (Kobayashi and Ishikawa 2019). Such seasonal-scaled positive upper-tropospheric geopotential height anomalies over northern China can contribute to the enhanced diffluence and deceleration of the basic flow near the STJ exit region. This indicates that there exists the possibility of relationships between the seasonally scaled anomalous circulation over north China and

HR18. This issue should be further investigated.

5. Summary and conclusions

To examine statistical large-scale atmospheric characteristics during the past heavy rainfall events that occurred widely in western Japan since 1979, we conducted a composite analysis of atmospheric fields. The results show that during these heavy rainfall events, the atmospheric fields are characterized by the upper-tropospheric trough over the KP, the upper-tropospheric ridge to the east of Japan, the surface high-pressure system to the southeast of Japan, and lower-tropospheric southwesterly moisture flux. Results of the composite analysis also indicate that clear RWPP along the PFJ over Siberia tends to occur just before the stronger heavy rainfall events, such as those of TP10, and contributes to the enhanced upper-tropospheric trough and ridge around Japan.

Further analysis considering various time-scale variabilities reveals that surface high-pressure anomalies to the southeast of Japan are dominated by variability with a 25–90-day period, which are generally enhanced by the RWPP along the PFJ. These are also likely enhanced by convective activity around the Philippines in association with the northward migration of the active phase of the BSISO. However, variability with an 8–25-day period dominates lower-pressure anomalies over the ECS in relation to the development of the upper-tropospheric trough around the KP.

We also investigated the atmospheric fields during HR18. The atmospheric features during HR18 are generally similar to those of the other heavy rainfall events. The RWPP along the PFJ enhances the surface high-pressure system to the southeast of Japan for both HR18 and TP10. It is noteworthy that the surface high-pressure systems to the southeast of Japan were dominated by 25–90-day period variabilities for both HR18 and TP10. During HR18, in addition to the RWPP along the PFJ, a remarkable RWPP occurred along the STJ in late June 2018 that intensified the surface high-pressure system to the southeast of Japan.

We further discussed another effect of this remarkable RWPP in late June along the STJ. Results of our analysis indicate that the low-pressure system with a 8–25-day period develops to the south of Japan in association with wave breaking induced by the remarkable RWPP in late June along the STJ. This wave breaking leads to the southward penetration of positive PV anomalies accompanied by negative potential temperature anomalies in the tropopause. This leads to thermodynamically unstable atmospheric conditions and activates convection around 20°N, 140°E, which then propagates northwestward toward the ECS accompanied by the surface low-pressure system just before HR18. Consequently, the simultaneous development of both the high-pressure system to the southeast of Japan and the low-pressure system over the ECS contributed to the extreme southerly moisture flux into western Japan.

During HR18, the sharp upper-tropospheric trough was observed over the KP. We found that high frequency variability with a period shorter than 8 days is predominant in this trough.

We discussed the mechanism for the predominance of higher frequency variability over the KP, comparing the longitudinal gradient of 200-hPa zonal winds filtered using a 90-day LPF from northern China to the KP among the heavy rainfall events over western Japan. We found that during HR18, the significant deceleration of the basic flow around 115°E compared with those in the other events contributed to the stagnation and amplification of Rossby waves.

Finally, as described in section 3.2, we found that the direct contribution of the BSISO to the development of the surface high-pressure system to the southeast of Japan during HR18 is less than during the other analyzed events because the active phase of the BSISO is located south of 10°N and far from the surface high-pressure system to the southeast of Japan. However, in mid-June 2018, the northward migration of the amplified active phase of the BSISO was clearly observed (not shown). The role of intra-seasonal variability in the excitation of quasi-stationary Rossby waves that propagate in the mid-latitudes of the Northern Hemisphere should be further investigated. In addition, it remains unclear how such a remarkable RWPP along the STJ in late June was excited. The mechanisms driving extreme events, including heavy rainfall and heat waves, around Japan also warrant further consideration.

Supplement

Figure S1 in supplement shows scatter diagrams of regionally averaged (31.25°−35°N, 130°−135°E) 3-day mean anomaly fields of water vapor flux divergence in the lower troposphere for days representing 3-day precipitation peaks during the heavy rainfall events over western Japan that exceed the 95th percentile. The decomposition of water vapor flux is based on equation (2) in Sekizawa et al. (2019). The red and orange circles represent HR18 and TP10, respectively.

Figure S2 in supplement is as in Fig. S1 but for regionally averaged (30°−45°N, 60°−120°E) zonal components of 200−hPa WAF 8 days before 3-day precipitation peaks during heavy rainfall events over western Japan that exceed the 95th percentile.

Figure S3 in supplement is as in the left panels of Fig. 8 but for (left) MD10 and (right) LW10.

Figure S4 in supplement is as in Figs. 9g and 9o but for from 12 days to 3 days before 3-day precipitation peaks during TP10 (a-d) and HR18 (e-h). The contour interval is 5 W m^{-2}.

Sekizawa, S., and co-authors, 2019: Anomalous moisture transport and oceanic evaporation during a torrential rainfall event over western Japan in early 2018. *SOLA*, **15A**, 25-30.

Acknowledgments

The authors are grateful to the anonymous reviewers for their constructive comments and advice. The JRA-55 dataset used in this paper is publicly available on the JMA Data Dissemination System (http://jra.kishou.go.jp/JRA-55/index_en.html) and from collaborative organizations (detailed information is available on the JRA-55 website). NOAA Interpolated OLR data were downloaded from the U.S. NOAA Earth System Research Laboratory. AMeDAS daily precipitation was downloaded from JMA. We are also thankful to Mr. Kazuya Yamashita of JMA for helping us obtain JMA's observation data.

References

Akiyama, T., 1975: Southerly transversal moisture flux into the extremely intense rainfall zone in the Baiu season. *J. Meteor. Soc. Japan*, **53**, 304-316.

Akiyama, T., 1984: A medium-scale cloud cluster in a Baiu front. Part I Evolution process and fine structure. *J. Meteor. Soc. Japan*, **62**, 485-504.

Akiyama, T., 1989: Large, synoptic and meso-scale variations of the Baiu front during July 1982. Part I Cloud features. *J. Meteor. Soc. Japan*, **67**, 57-81.

Duchon, C. E., 1979: Lanczos filtering in one and two dimensions. *J. Appl. Meteor.*, **18**, 1016-1022.

Enomoto, T., B. J. Hoskins and Y. Matsuda, 2003: The formation mechanism of the Bonin high in August. *Quart. J. Roy. Meteor. Soc.*, **129**, 157-178.

Enomoto, T., 2019: Influence of the track forecast of typhoon Prapiroon on the heavy rainfall in western Japan in July 201*8. SOLA, 15A, 66-71, https://doi.org/10.2151/sola.15A-012.*

Hirota, N., and M. Takahashi, 2012: A tripolar pattern as an internal mode of the East Asian summer monsoon. Climate Dynamics, 39, 2219-2238.

Hirota, N., Y. N. Takayabu, M. Kato, and S. Arakane, 2016: Roles of an atmospheric river and a cutoff low in the extreme precipitation event in Hiroshima on 19 August 2014. *Mon. Wea. Rev.*, **144**, 1145–1160, https://doi.org/10.1175/MWR-D-15-0299.1.

Iwao, K., and M. Takahashi, 2008: A precipitation seesaw mode between northeast Asia and Siberia in summer caused by Rossby waves over the Eurasian continent. *J. Climate*, **21**, 2401–2419.

Kamae, Y., W. Mei, and S.-P. XIE, 2017: Climatological relationship between warm season atmospheric rivers and heavy rainfall over East Asia. *J. Meteor. Soc. Japan*, **95**, 411–431, https://doi.org/10.2151/jmsj.2017-027.

Kamahori, H., 2012: Mean features of tropical cyclone precipitation from TRMM/3B42. *SOLA*, **8**, 17-20, https://doi.org/10.2151/sola.2012-005.

Kato, T., and H. Goda, 2001: Formation and maintenance processes of a stationary band-shaped heavy rainfall observed in Niigata on 4 August 1998. *J. Meteor. Soc. Japan*, **79**, 899–924.

Kikuchi, K., B. Wang, and Y. Kajikawa, 2012: Bimodal representation of the tropical intraseasonal oscillation. *Climate Dynamics*, **38**, 1989–2000. https://doi.org/10.1007/s00382-011-1159-1.

Kobayashi, C., and I. Ishikawa, 2019: Prolonged northern-mid-latitude tropospheric warming in 2018 well predicted by the JMA operational seasonal prediction system. *SOLA*, 15A, 31-36, https://doi.org/10.2151/sola.15A-006.

Kobayashi, S., Y. Ota, Y. Harada, A. Ebita, M. Moriya, H. Onoda, K. Onogi, H. Kamahori, C. Kobayashi, H. Endo, K. Miyaoka, and K. Takahashi, 2015: The JRA-55 Reanalysis: General specifications and basic characteristics. *J. Meteor. Soc. Japan*, **93**, 5-48, https://doi.org/10.2151/jmsj.2015-001.

Kosaka, Y., and H. Nakamura, 2010: Mechanisms of meridional teleconnection observed between a summer monsoon system and a subtropical anticyclone. Part I: The Pacific-Japan pattern. *J. Climate*, **23**, 5085−5108.

Kosaka, Y., S.-P. Xie, and H. Nakamura, 2011: Dynamics of Interannual variability in summer precipitation over East Asia. *J. Climate*, **24**, 5435−5453.

Liebmann, B., and C. A. Smith, 1996: Description of a complete (interpolated) outgoing longwave radiation dataset. *Bull. Amer. Meteor. Soc.*, **77**, 1275-1277.

Nakamura, H., and T. Fukamachi, 2004: Evolution and dynamics of summertime blocking over the Far East and the associated surface Okhotsk high. Quart. *J. Roy. Meteor. Soc.*, **130**, 1213–1233.

Nakamura, N., and C. S. Y. Huang, 2017: Local wave activity and the onset of blocking along a potential vorticity front. *J. Atmos. Sci.*,**74**, 2341-2361, https://doi.org/10.1175/JAS-D-17-0029.1.

Ninomiya, K., 1978: Heavy rainfalls associated with frontal depression in Asian subtropical humid region (I) synoptic-scale features. *J. Meteor. Soc. Japan*, **56**, 253-266.

Ninomiya, K., 1984: Characteristics of Baiu front as a predominant subtropical front in the summer northern hemisphere. *J. Meteor. Soc. Japan*, **62**, 880-894.

Ninomiya, K., and T. Akiyama 1992: Multi-scale features of Baiu, the summer monsoon over Japan and the East Asia. *J. Meteor. Soc. Japan*, **70**, 467-495.

Ninomiya, K., 2001: Large λ-shaped cloud zone formed around 6 July 1991 with pole-ward moisture transport from intense rainfall area in Meiyu-Baiu front. *J. Meteor. Soc. Japan*, **79**, 805-813.

Ninomiya, K., and Y. Shibagaki, 2007: Multi-scale of the Meiyu-Baiu front and associated precipitation systems. *J. Meteor. Soc. Japan*, **85B**, 103-122.

Nitta, T., 1987: Convective activities in the tropical western Pacific and their impact on the Northern Hemisphere summer circulation. *J. Meteor. Soc. Japan*, **65**, 373−390, https://doi.org/10.2151/jmsj1965.65.3_373.

Ogasawara, T., and R. Kawamura, 2008: Effects of combined teleconnection patterns on the East Asian summer monsoon circulation: remote forcing from low- and high-latitude regions. *J. Meteor. Soc. Japan*, **86**, 491–504.

Shibagaki, Y., and K. Ninomiya, 2005: Multi-scale interaction processes associated with development of a sub-synoptic scale depression on the Meiyu-Baiu frontal zone. *J. Meteor. Soc. Japan*, **83**, 219-236.

Shimpo, A., and co-authors, 2019: Primary factors behind the Heavy Rain Event of July 2018 and the subsequent heat wave in Japan. *SOLA*, **15A**, 13-18.

Shutts, G. J., 1983: Propagation of eddies in diffluent jetstreams: Eddy forcing of 'blocking' flow fields. Quart. *J. Roy. Meteor. Soc.*, **109**, 737–761, doi:10.1002/qj.49710946204.

Takaya, K., and H. Nakamura, 2001: A formulation of a phase- independent 12 wave-activity flux for stationary and migratory quasi-geostrophic eddies on a 13 zonally varying basic flow. *J. Atmos. Sci.*, **58**, 608−627.

Takemura, K., S. Wakamatsu, H. Togawa, A. Shimpo, C. Kobayashi, S. Maeda, and H. Nakamura, 2019: Extreme moisture flux convergence of western Japan during the heavy rain event of July 2018. *SOLA,* **15A**, 49-54.

Tsuguti, H., N. Seino, H. Kawase, Y. Imada, T. Nakaegawa, and I. Takayabu, 2018: Meteorological overview and mesoscale characteristics of the Heavy Rain Event of July 2018 in Japan. *Landslides*, https://doi.org/10.1007/s10346-018-1098-6.

Yokoyama, C., H. Tsujii, and Y. N. Takayabu, 2020: The effects of an upper-tropospheric trough on the heavy rainfall event in July 2018 over Japan, *J. Meteor. Soc. Japan*, **98**(1), 235-255. https://doi:10.2151/jmsj.2020-013.

Yoshida, K., and H. Ito, 2012: Indirect effects of tropical cyclones on heavy rainfall events in Kyushu, Japan, during the Baiu season. *J. Meteor. Soc. Japan*, **90**, 377-401, https://doi: 10.2151/jmsj.2012-303.

List of Figures

Fig. 1. Ranking of 3-day precipitation averaged over western Japan that exceeds the 95th percentile during warm seasons (May–September) from 1979 to 2018. Gray bars indicate events during which typhoon centers existed within 500 km from observational stations in western Japan. Colors identify specific events discussed in the text.

Fig. 2. Composite maps of 3-day mean anomaly fields of (a) 200-hPa relative vorticity (10^{-6} s^{-1}), (b) 200-hPa zonal wind (m s^{-1}), (c) 500-hPa vertical velocity (10^{-2} Pa s^{-1}), (d) 500-hPa geopotential height (gpm), (e) 850-hPa relative vorticity (10^{-6} s^{-1}), (f) SLP (hPa), (g) total-column water vapor flux (vector, kg m s^{-1}) and its divergence (contours, 10^{-4} kg s^{-1}), and (h) OLR (W m^{-2}) for days representing 3-day precipitation peaks of TP10. The contour intervals are (a, e) 8×10^{-6} s^{-1}, (b) 4 m s^{-1}, (c) 4×10^{-2} Pa s^{-1}, (d) 20 gpm, (f) 1 hPa, (g) 0.6×10^{-4} kg s^{-1}, and (h) 10 W m^{-2}. Light and dark shading indicates areas above the 90% and 95% confidence levels, and pink and blue colors indicate positive and negative signs, respectively. The vector scales at the bottom of the panels denote vectors of total-column water vapor flux. The tone bar at the lower-left corner of the panels represents the color scale for the vector corresponding to the magnitude of total-column water vapor flux.

Fig. 3. As in Fig. 2 but for WAF (vectors, m^2 s^{-2}) and geopotential height anomalies

(contours, gpm) at 250 hPa from 9 days before (top panel) to the day of 3-day precipitation peaks (bottom panel) of TP10. The contour interval is 20 gpm. WAFs are calculated from the composite fields. The vector scales at the bottom of the panels denote vectors of WAF. The tone bar at the lower-left corner of the panels represents the color scale for the vector corresponding to the magnitude of WAF.

Fig. 4. As in Fig. 3 but for MD10 (a–d) and LW10 (e–h).

Fig. 5. Three-day mean anomaly fields for (a) 200-hPa relative vorticity (10^{-6} s^{-1}), (b) 200-hPa zonal wind (m s^{-1}), (c) 500-hPa vertical velocity (10^{-2} Pa s^{-1}), (d) 500-hPa geopotential height (gpm), (e) 850-hPa relative vorticity (10^{-6} s^{-1}), (f) SLP (hPa), (g) total-column water vapor flux (vector, kg m s^{-1}) and its divergence (shading, 10^{-4} kg s^{-1}), and (h) OLR (W m^{-2}) during 5–7 July 2018. The vector scales at the bottom of the panels denote vectors of total-column water vapor flux. The tone bar at the lower-left corner of the panels represents the color scale for the vector corresponding to the magnitude of total-column water vapor flux.

Fig. 6. Scatter diagrams of regionally averaged 3-day mean anomaly fields for (a) SLP (hPa), (b) 925-hPa meridional winds (m s^{-1}), (c) 925-hPa specific humidity (10^{-3} kg kg^{-1}),

(d) 925-hPa meridional component of water vapor flux (10^{-2} kg kg^{-1} m s^{-1}), and (e) total-column water vapor flux divergence (10^{-4} kg s^{-1}), for days representing 3-day precipitation peaks during the heavy rainfall events over western Japan that exceed the 95th percentile. Red, orange and gray circles represent HR18, TP10 and the other events, respectively.

Fig. 7. WAF (vectors, m^2 s^{-2}) and geopotential height anomalies (shading, gpm) at 250 hPa for (a) 26–28 June, (b) 29 June–1 July, (c) 2–4 July, and (d) 5–7 July 2018. The vector scales at the bottom of the panels denote vectors of WAF. The tone bar at the lower-left corner of the panels represents the color scale for the vector corresponding to the magnitude of WAF.

Fig. 8. (a–d) Composite maps of time-filtered SLP anomaly fields (hPa) for TP10 and (e–h) time-filtered SLP anomaly fields on 6 July 2018 using (a),(e) an 8-day HPF, (b),(f) an 8–25-day BPF, (c),(g) a 25–90-day BPF, and (d),(h) a 90-day LPF. The contour interval in (a–d) is 1 hPa. Light and dark shadings in (a–d) indicate areas above the 90% and 95% confidence levels, respectively.

Fig. 9. As in Fig. 8 but for (a–d and i–l) 250-hPa geopotential height and (e–h and m–p)

OLR. The contour intervals are (a–d) 20 gpm and (e–h) 5 W m^{-2}.

Fig. 10. 8–25-day BPF SLP anomalies (contour, hPa) and OLR anomalies (shading, W m^{-2}) from 26 June to 6 July 2018. The contour interval is 1 hPa.

Fig. 11. As in Fig. 8 but for time-filtered 360-K PV anomalies (PVU) using (a and d) 8-day HPF, (b and e) 8–25-day BPF, and (c and f) 25-day LPF. The contour interval is 0.5 PVU. [Units: PVU (1 PVU = 10^{-6} m^2 s^{-1} K kg^{-1})].

Fig. 12. As in Fig. 6 but for the regional maximum PV anomaly (PVU) at 360 K in the region (30°−50°N, 110°−130°E) using (a) an 8-day HPF, (b) an 8−25-day BPF, and (c) a 25-day LPF. [Units: PVU (1 PVU = 10^{-6} m^2 s^{-1} K kg^{-1})].

Fig. 13. Daily-mean (a) PV at 360 K (PVU), (b) potential temperature anomaly at 2 PVU (K), (c) Longitude-pressure cross section of the square of Brunt-Vaisälä frequency (N^2) anomaly (10^{-5} s^{-2}), (d) longitudinal distribution of latitudinally (15°–20°N) and vertically (300–150 hPa) averaged N^2 anomaly (10^{-5} s^{-2}), (e) OLR anomalies (W m^{-2}) on 25 June 2018. Contours and shading in (b) indicate actual values and anomalies, respectively. The contour interval in (b) is 5 K for values ≥355 K. [Units: PVU (1 PVU = 10^{-6} m^2 s^{-1} K kg^{-1})].

Fig. 14. Instantaneous 6-hourly PV map at 360 K from (a) 12 UTC 5 July 2018 to (h) 06 UTC 7 July 2018. [Units: PVU (1 PVU = 10^{-6} m^2 s^{-1} K kg^{-1})].

Fig. 15. (a) 90−day LPF 200−hPa zonal wind field on 6 July 2018 and (b) the distribution of the longitudinal gradient of the 90−day LPF 200−hPa zonal wind component (10^{-6} m s^{-1}

m^{-1}) averaged over 35°–50°N for days representing 3-day precipitation peaks during the heavy rainfall events over western Japan that exceed the 95th percentile. Gray lines indicate individual cases. The red line indicates HR18. Blue and black lines represent the average of the heavy rainfall events over western Japan and the climatological mean, respectively.

List of Tables

Table 1. List of top 21 extreme heavy rainfall events in western Japan. Zero value of typhoon flag means that any center of typhoon does not exist within 500 km from the stations in western Japan. Gray shadings indicate exclusion from composite analysis. The dates represent the central dates for 3-day summation of precipitation.

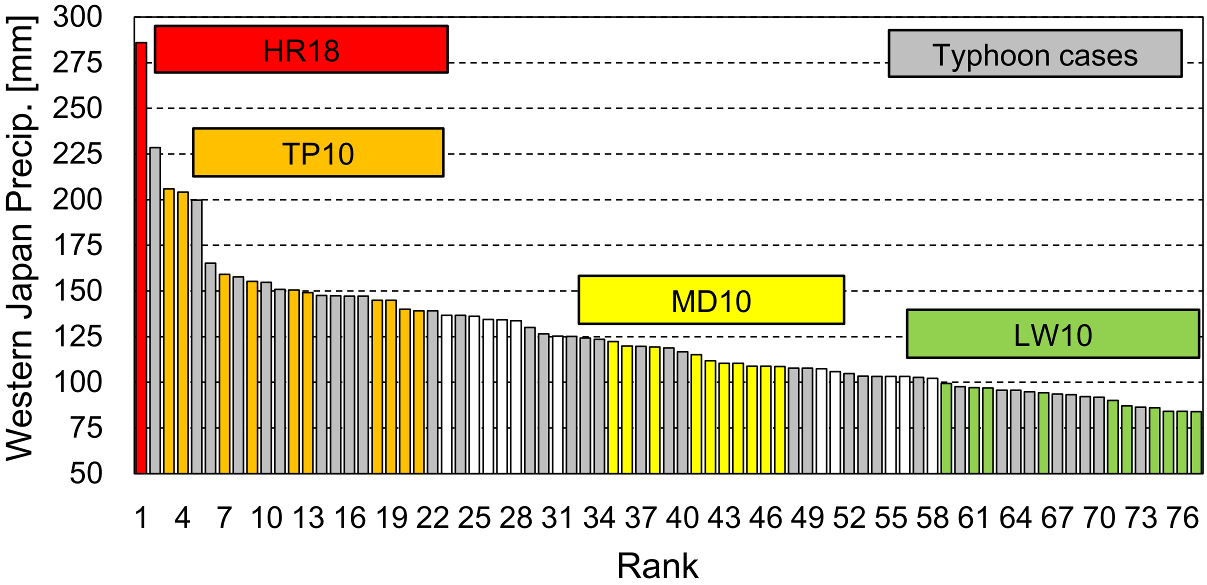

Fig. 1. Ranking of 3-day precipitation averaged over western Japan which exceeds the 95th percentile during the warm seasons (May-September) from 1979 to 2018. Gray bars indicate events during which typhoon centers existed within 500 km from observational stations in western Japan. Colors identify specific events discussed in the text.

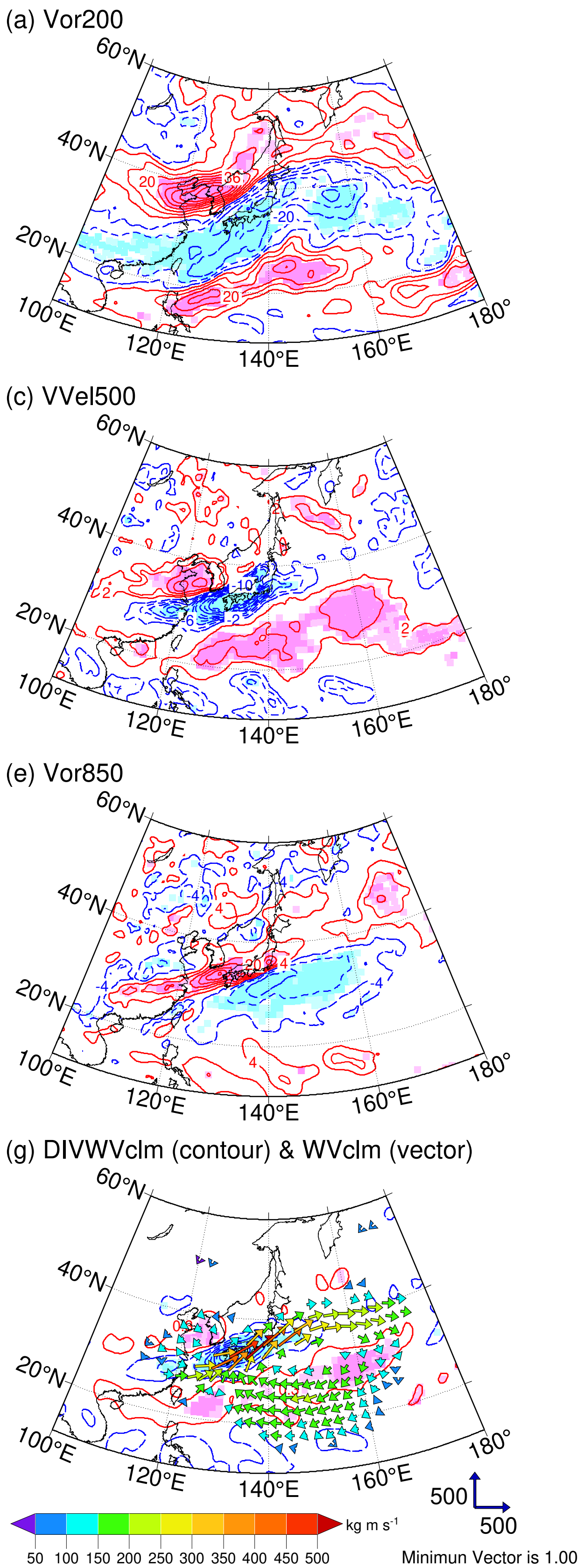

Fig. 2. Composite maps of 3-day mean anomaly fileds of (a) 200-hPa relative vorticity (10^{-6} s^{-1}), (b) 200-hPa zonal wind (m s^{-1}), (c) 500-hPa vertical velocity (10^{-2} Pa s^{-1}), (d) 500-hPa geopotential height (gpm), (e) 850-hPa relative vorticity (10^{-6} s^{-1}), (f) SLP (hPa), (g) total-column water vapor flux (vector, kg m s^{-1}) and its divergence (contours, 10^{-4} kg s^{-1}), and (h) OLR (W m^{-2}) for days representing 3-day precipitation peaks of TP10. The contour intervals are (a, e) 8×10^{-6} s^{-1}, (b) 4 m s^{-1}, (c) 4×10^{-2} Pa s^{-1}, (d) 20 gpm, (f) 1 hPa, (g) 0.6×10^{-4} kg s^{-1}, and (h) 10 W m^{-2}. Light and dark shading indicates areas above the 90% and 95% confidence levels, and pink and blue colors indicate positive and negative signs, respectively. The vector scales at the bottom of the panels denote vectors of total-column water vapor flux. The tone bar at the lower-left corner of the panels represents the color scale for the vector corresponding to the magnitude of total-column water vapor flux.

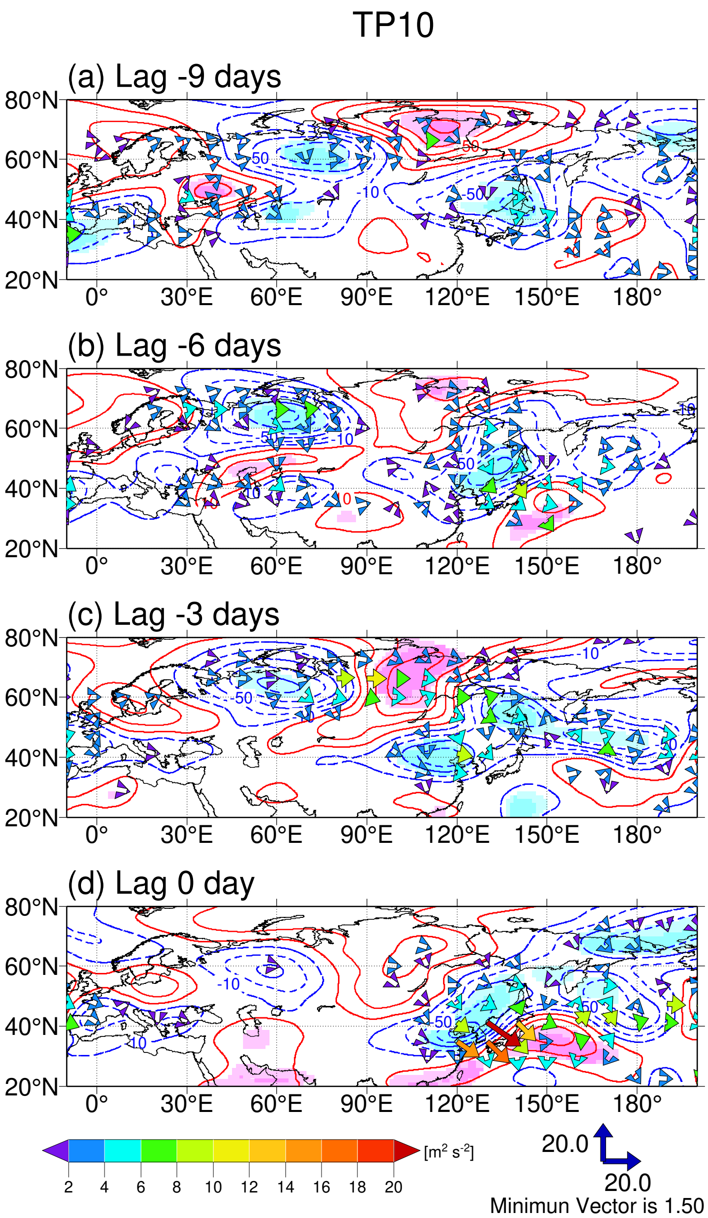

Fig. 3. As in Fig. 2 but WAF (vectors, m^2 s^{-2}) and geopotential height anomalies (contour, gpm) at 250 hPa from 9 days before (top panel) to the day of 3-day precipitation peaks (bottom panel) of TP10. The contour interval is 20 gpm. WAFs are calculated from the composite fields. The vector scales at the bottom of the panels denote vectors of WAF. The tone bar at the lower-left corner of the panels represents the color scale for the vector corresponding to the magnitude of WAF.

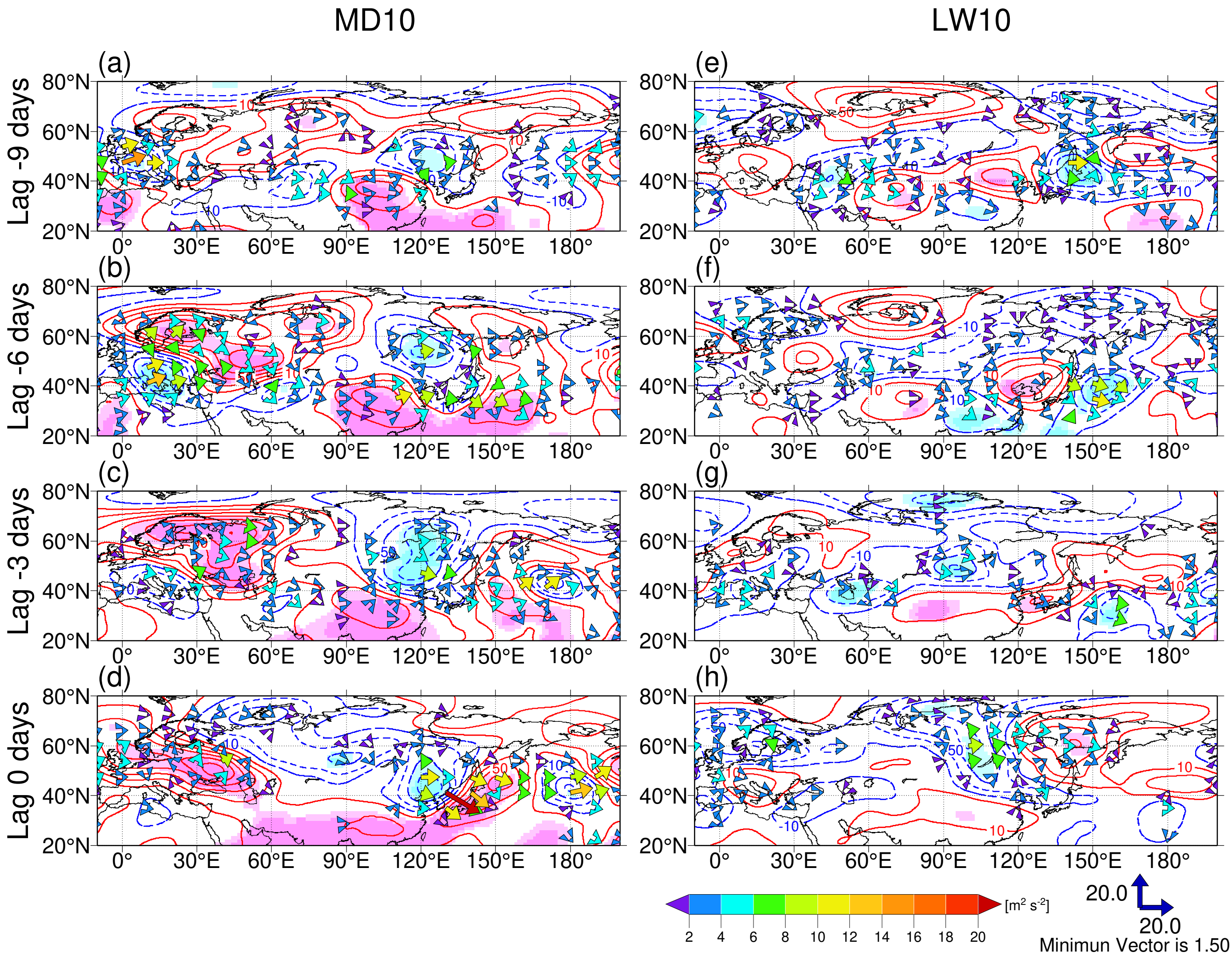

Fig. 4. As in Fig. 3 but for MD10 (a-d) and LW10 (e-h).

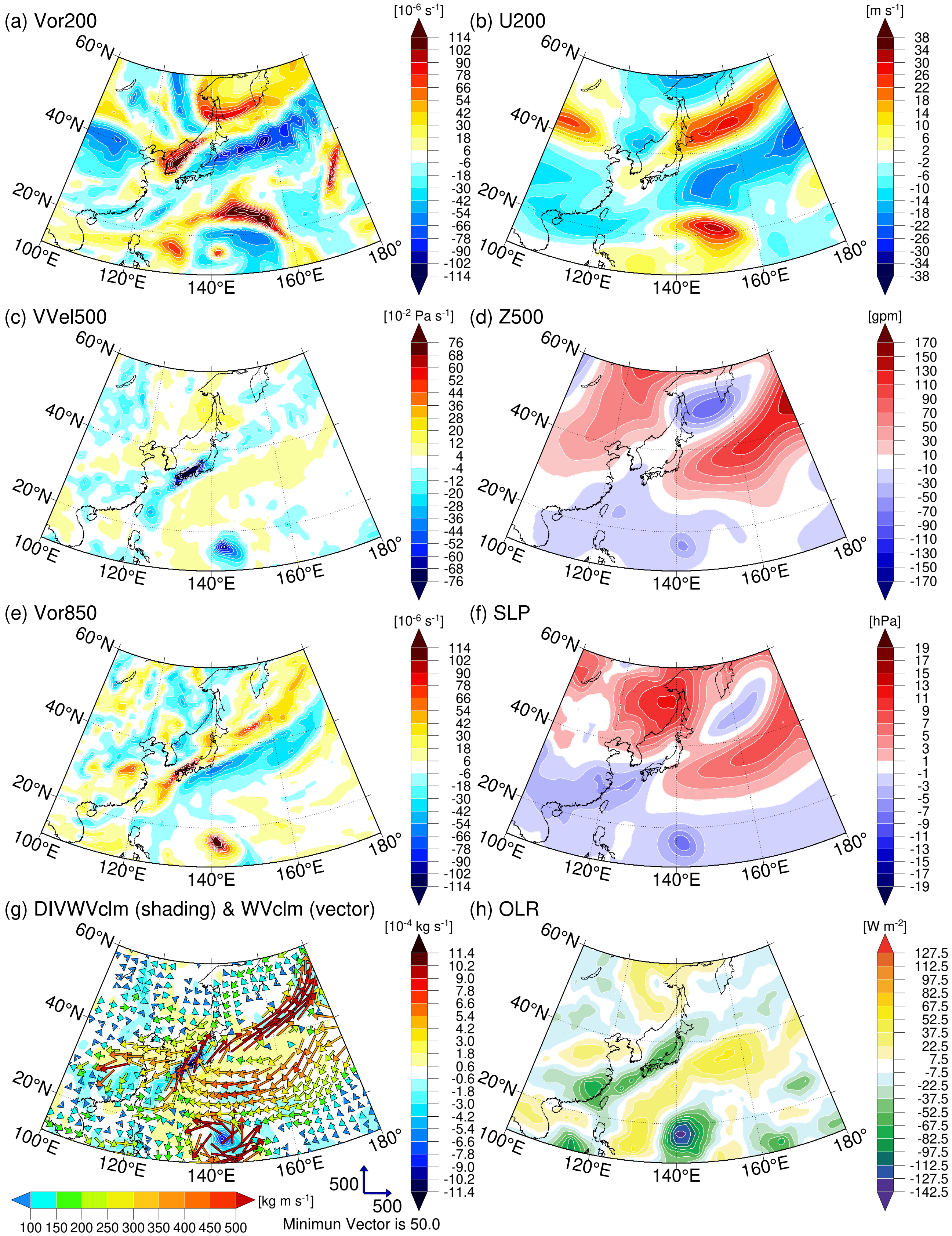

Fig. 5. Three-day mean anomaly fileds of (a) 200-hPa relative vorticity (10^{-6} s^{-1}), (b) 200-hPa zonal winds (m s^{-1}), (c) 500-hPa vertical velocity (10^{-2} Pa s^{-1}), (d) 500-hPa geopotential heights (gpm), (e) 850-hPa relative vorticity (10^{-6} s^{-1}), (f) SLP (hPa), (g) total column of water vapor flux (vector, kg m s^{-1}) and its divergence (shading, 10^{-4} kg s^{-1}), (h) OLR (W m^{-2}) during 5-7 July 2018.
The vector scales at the bottom of the panels denote vectors of total-column water vapor flux.
The tone bar at the lower-left corner of the panels represents the color scale for the vector corresponding to the magnitude of total-column water vapor flux.

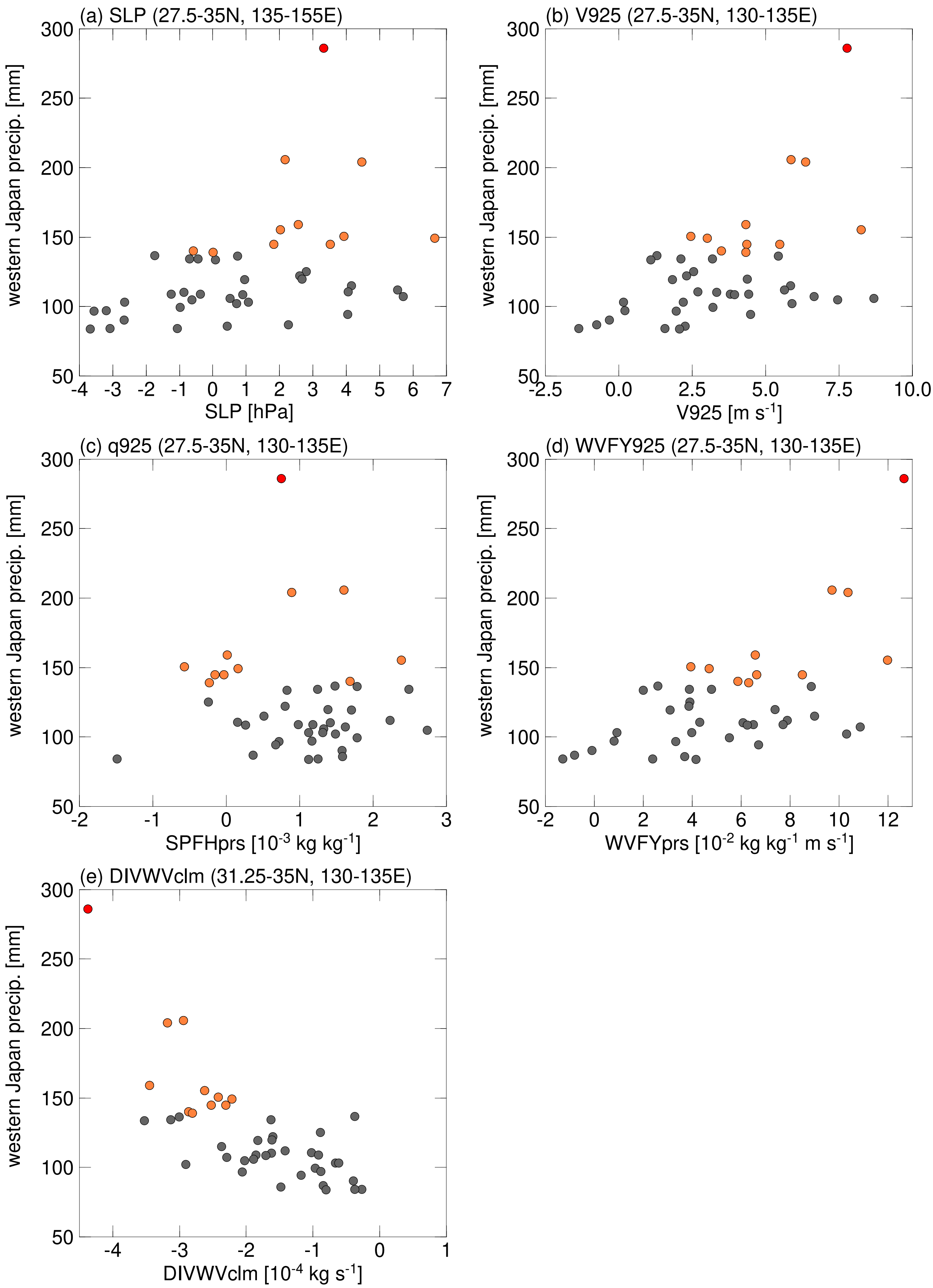

Fig. 6. Scatter diagrams of regional averaged 3-day mean anomaly fields for (a) SLP (hPa), (b) 925-hPa meridional winds (m s^{-1}), (c) 925-hPa specific humidity (10^{-3} kg kg^{-1}), (d) 925-hPa meridional component of water vapor flux (10^{-2} kg kg^{-1} m s^{-1}), and (e) total-column of water vapor flux divergence (10^{-4} kg s^{-1}), for days representing 3-day precipitation peaks during the heavy rainfall events over western Japan that exceed 95th percentile. Red, orange and gray circles represent HR18, TP10 and the other events, respectively.

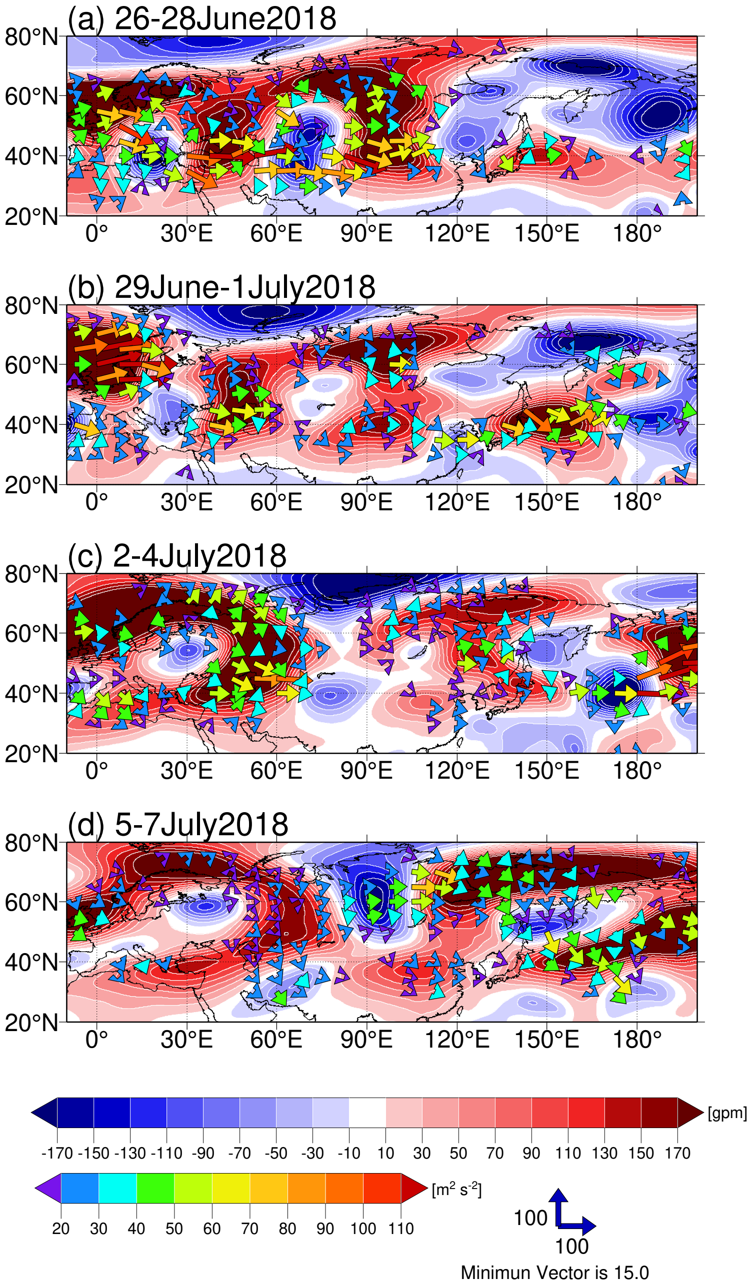

Fig. 7. WAF (vectors, $m^2\ s^{-2}$) and geopotential height anomalies (shading, gpm) at 250 hPa for (a) 26-28 June, (b) 29 June - 1July, (c) 2-4 July, and (d) 5-7 July 2018. The vector scales at the bottom of the panels denote vectors of WAF. The tone bar at the lower-left corner of the panels represents the color scale for the vector corresponding to the magnitude of WAF.

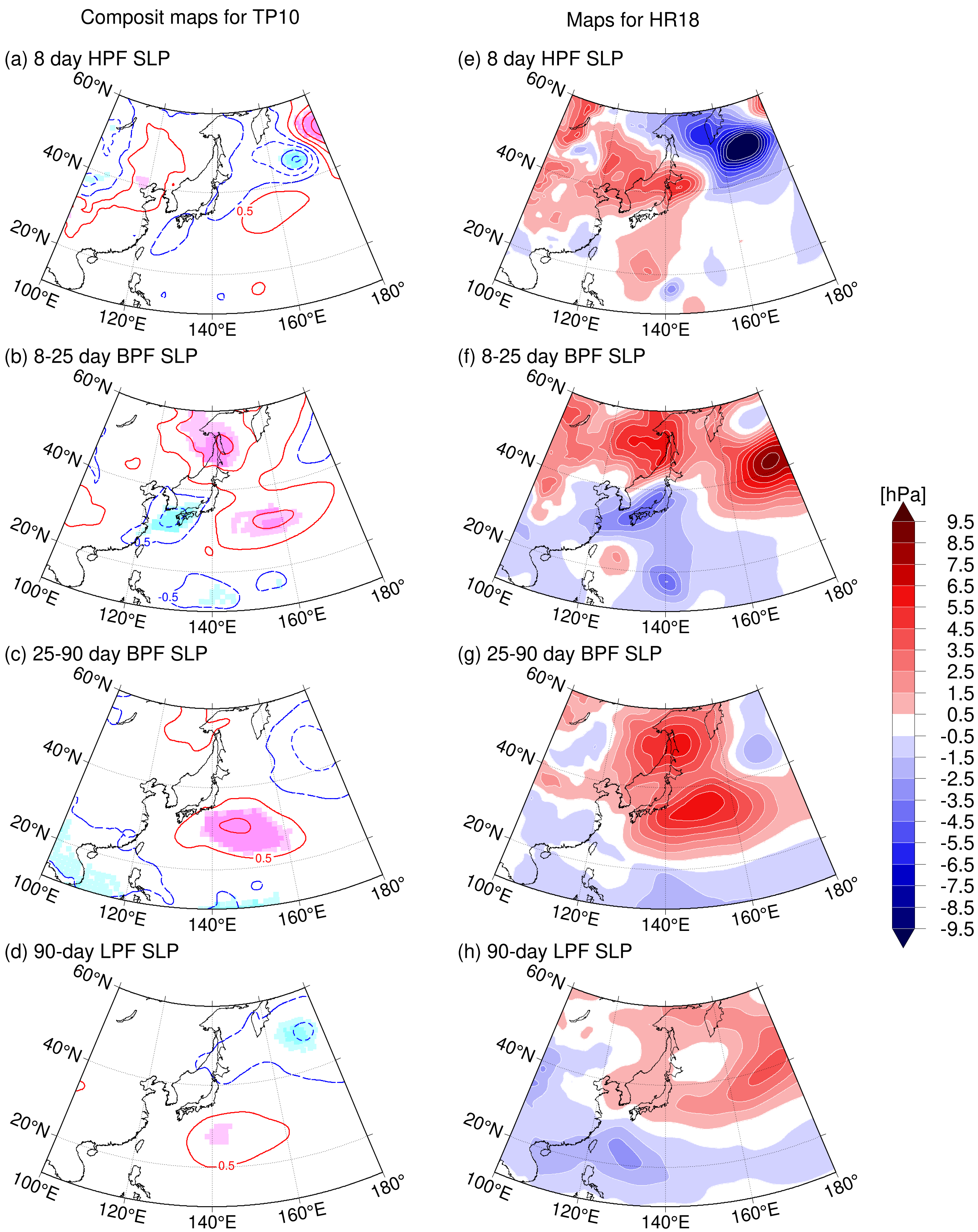

Fig. 8. (a-d) Composite maps of time-filtered SLP anomaly fields (hPa) for TP10 and (e-h) time-filtered SLP anomaly fields on 6 July 2018 using (a),(e) an 8-day HPF, (b),(f) an 8-25-day BPF, (c),(g) a 25-90-day BPF, and (d),(h) a 90-day LPF. The contour interval in (a-d) is 1 hPa. Light and dark shadings in (a-d) indicate areas above 90% and 95% confidence levels, respectively.

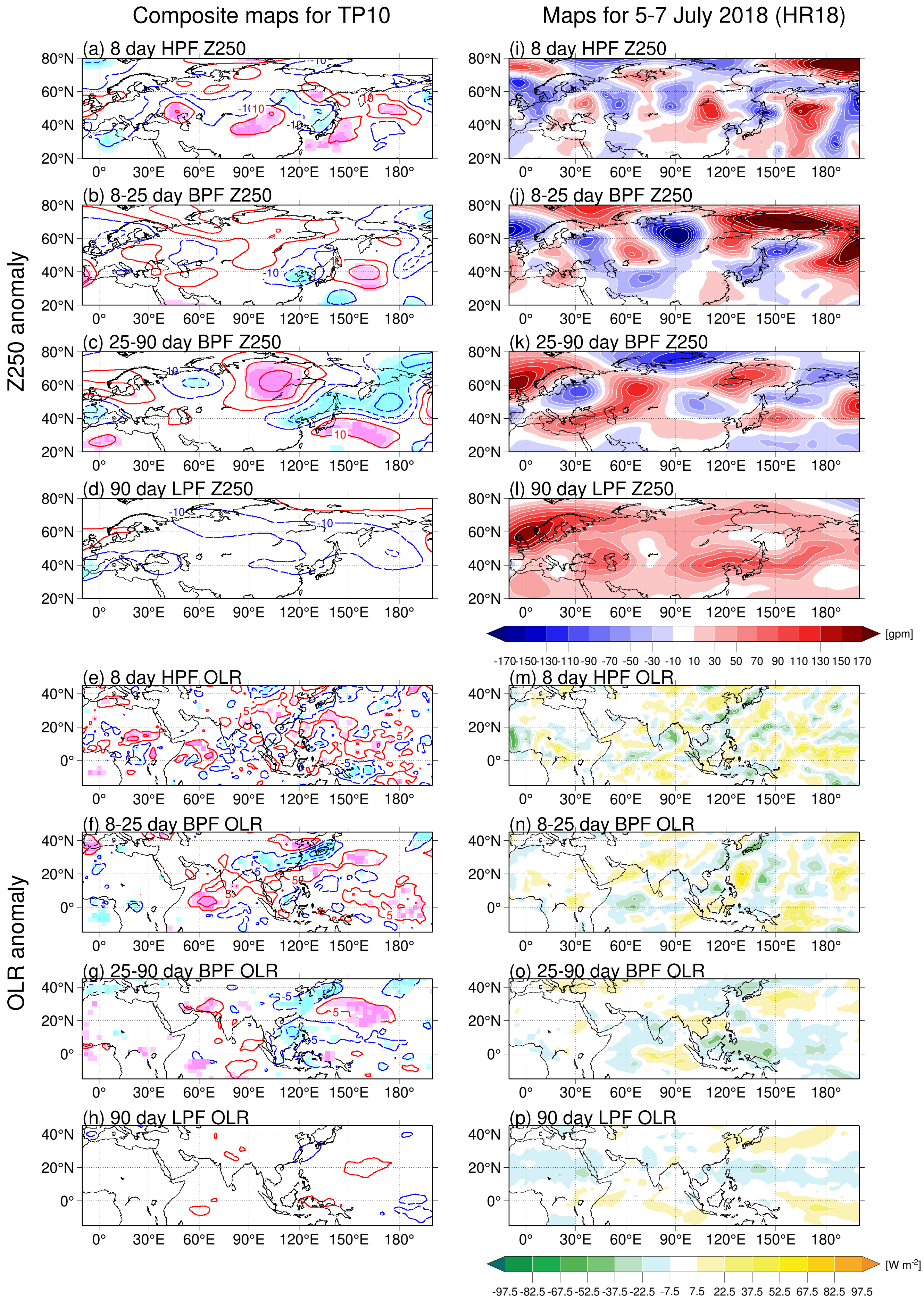

Fig. 9. As in Fig.8 but for (a-d and i-l) 250-hPa geopotential heights (gpm) and (e-h and m-p) OLR (W m^{-2}). The contour intervals are (a-d) 20 gpm and (e-h) 5 W m^{-2}.

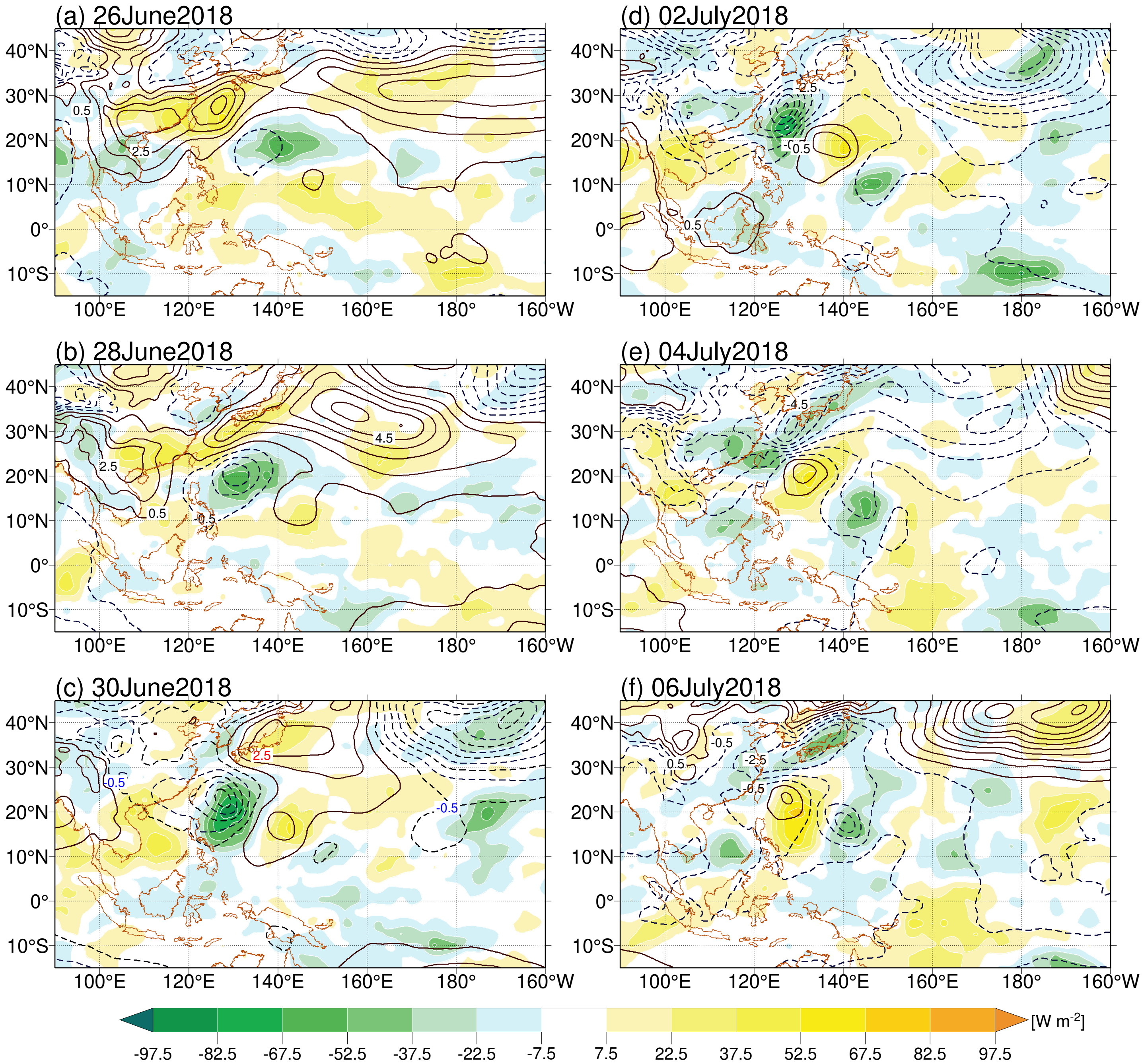

Fig. 10. 8-25 day BPF SLP anomalies (contour, hPa) and OLR anomalies (shading, W m^{-2}) from 26 June to 6 July 2018. The contour interval is 1 hPa.

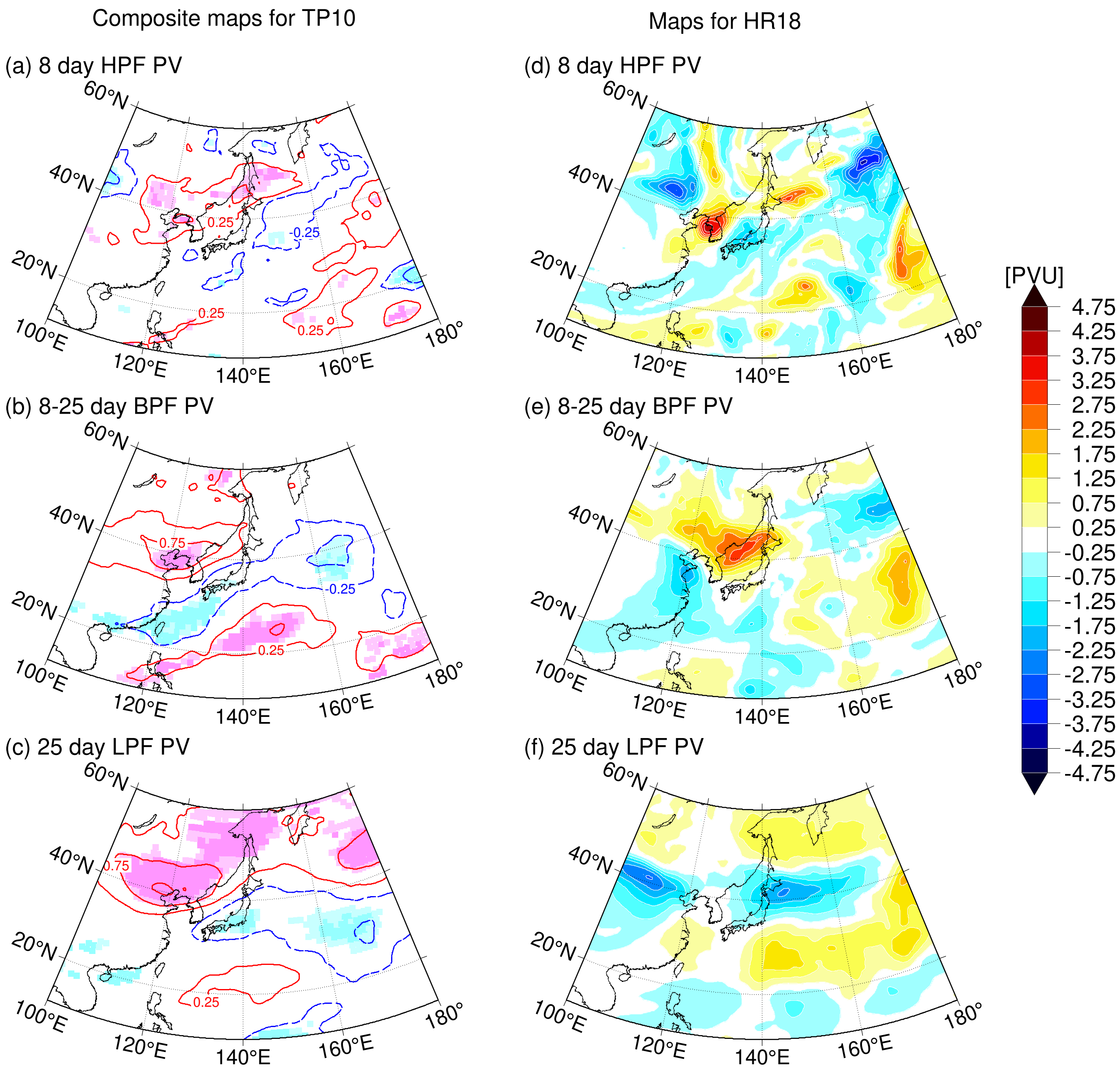

Fig. 11. As in Fig.8 but time-filtered 360-K PV anomalies (PVU) using (a and d) 8-day HPF, (b and e) 8-25 day BPF, and (c and f) 25-day LPF. The contour interval is 0.5 PVU. [Unit: PVU (1PVU=10^{-6} m^2 s^{-1} K kg^{-1})].

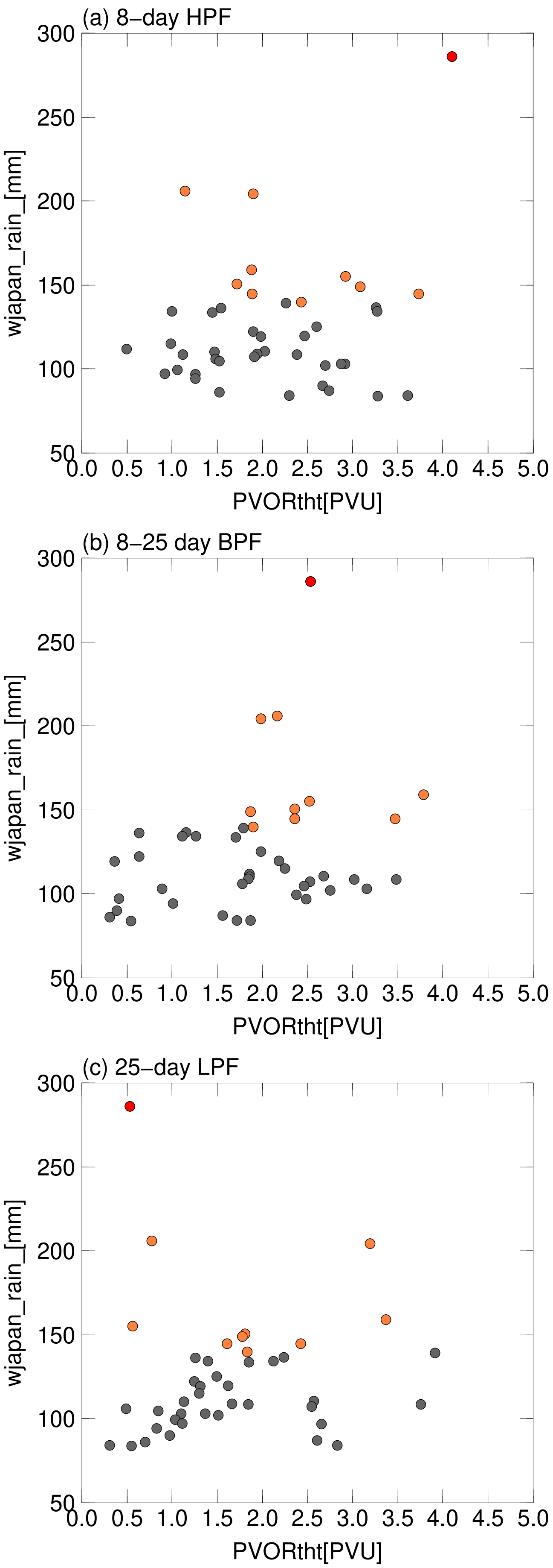

Fig. 12. As in Fig. 6 but for the regional maximum PV anomaly (PVU) at 360 K in the region (30−50N, 110−130E) using (a) an 8−day HPF, (b) an 8−25 day BPF, and (c) a 25−day LPF. [Unit: PVU (1PVU=10^{-6} m^2 s^{-1} K kg^{-1})].

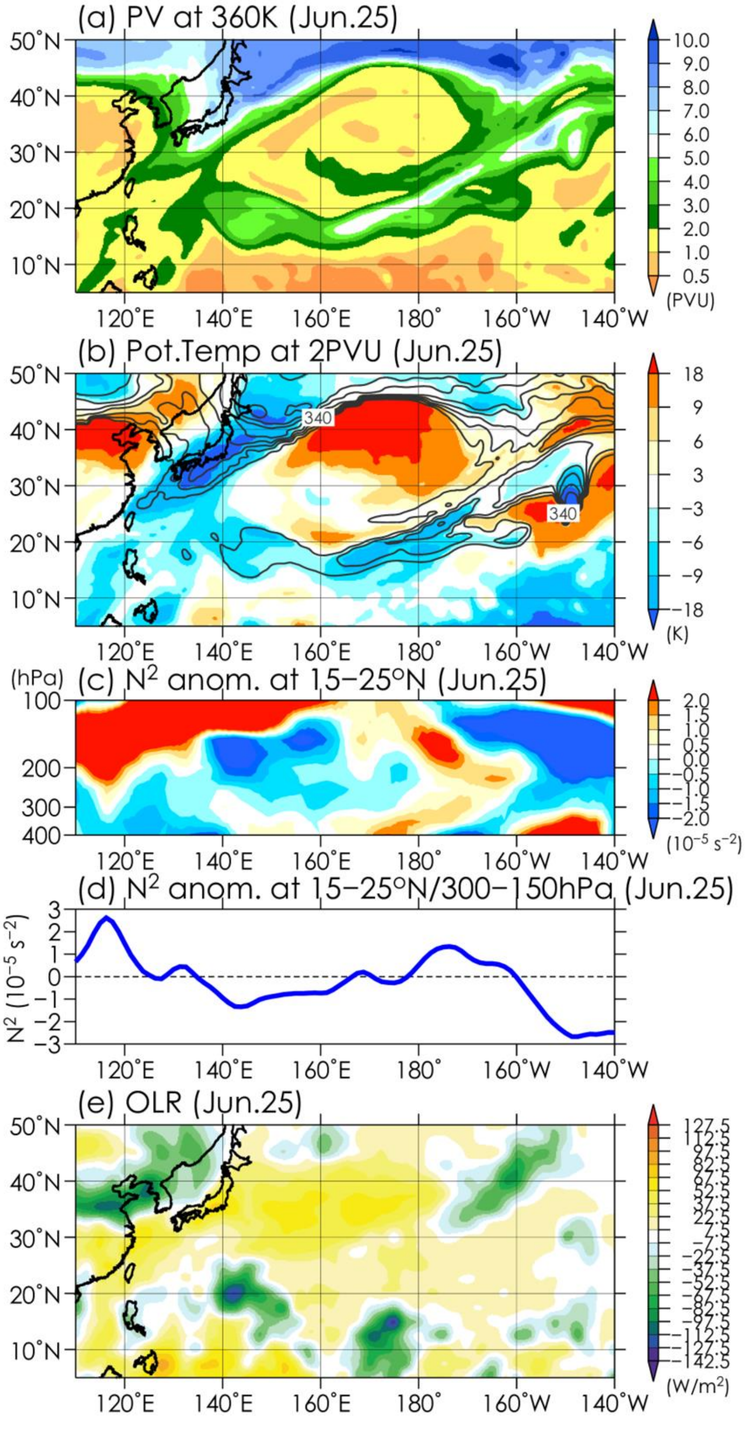

Fig. 13. Daily-mean (a) PV at 360 K (PVU), (b) potential temperature anomaly at 2 PVU (K), (c) Longitude-pressure cross section of the square of Brunt-Vaisälä frequency (N^2) anomaly (10^{-5} s^{-2}), (d) longitudinal distribution of latitudinally (15˚–20˚N) and vertically (300–150 hPa) averaged N^2 anomaly (10^{-5} s^{-2}), (e) OLR anomalies (W m^{-2}) on 25 June 2018. Contours and shading in (b) indicate actual values and anomalies, respectively. The contour interval in (b) is 5 K for values ≥355 K. [Units: PVU (1 PVU = 10^{-6} m^2 s^{-1} K kg^{-1})].

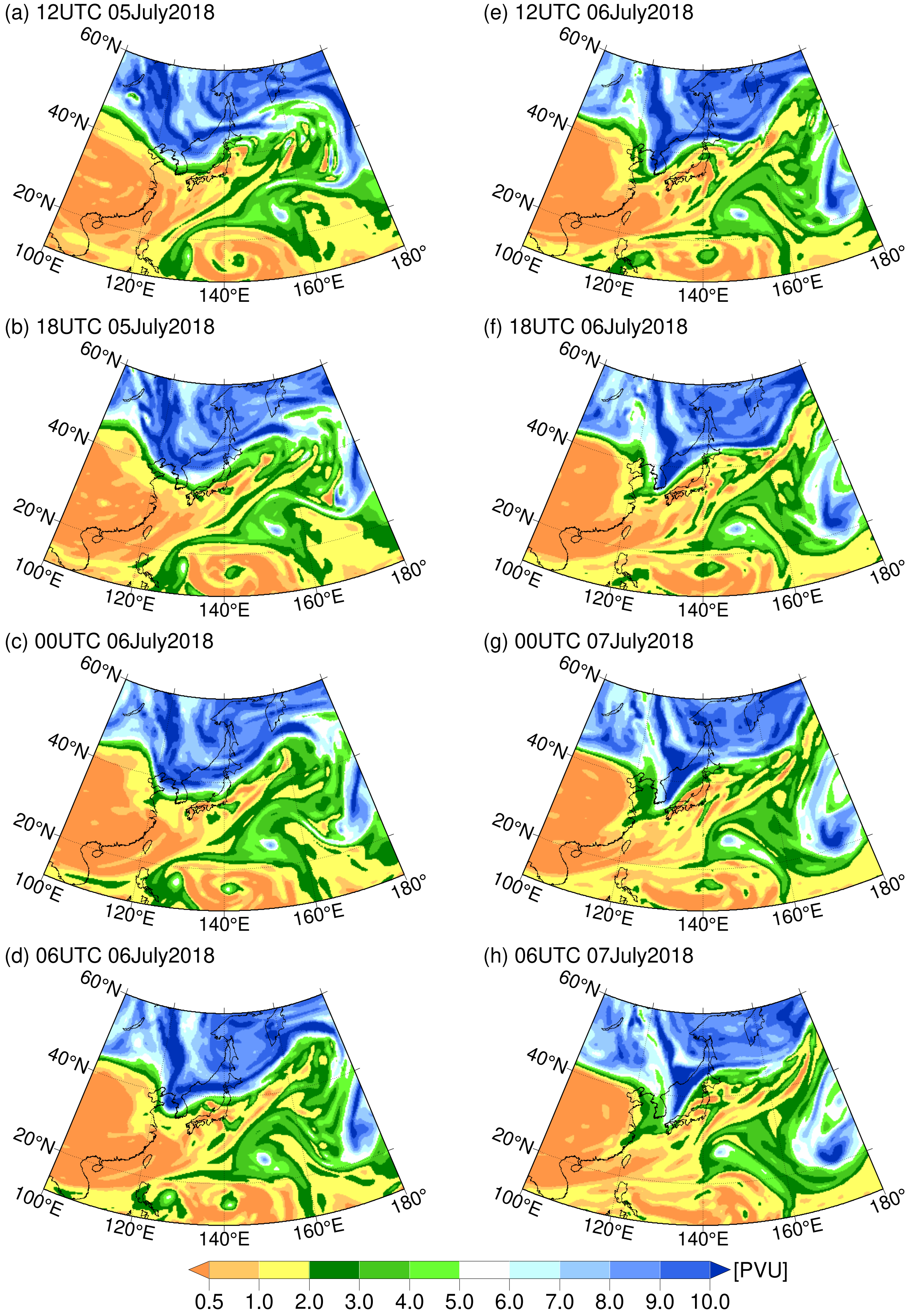

Fig. 14. Instantaneous 6-hourly PV map at 360 K from (a) 12 UTC 5 July 2018 to (h) 06 UTC 7 July 2018. [Unit: PVU (1PVU=10^{-6} m^2 s^{-1} K kg^{-1})].

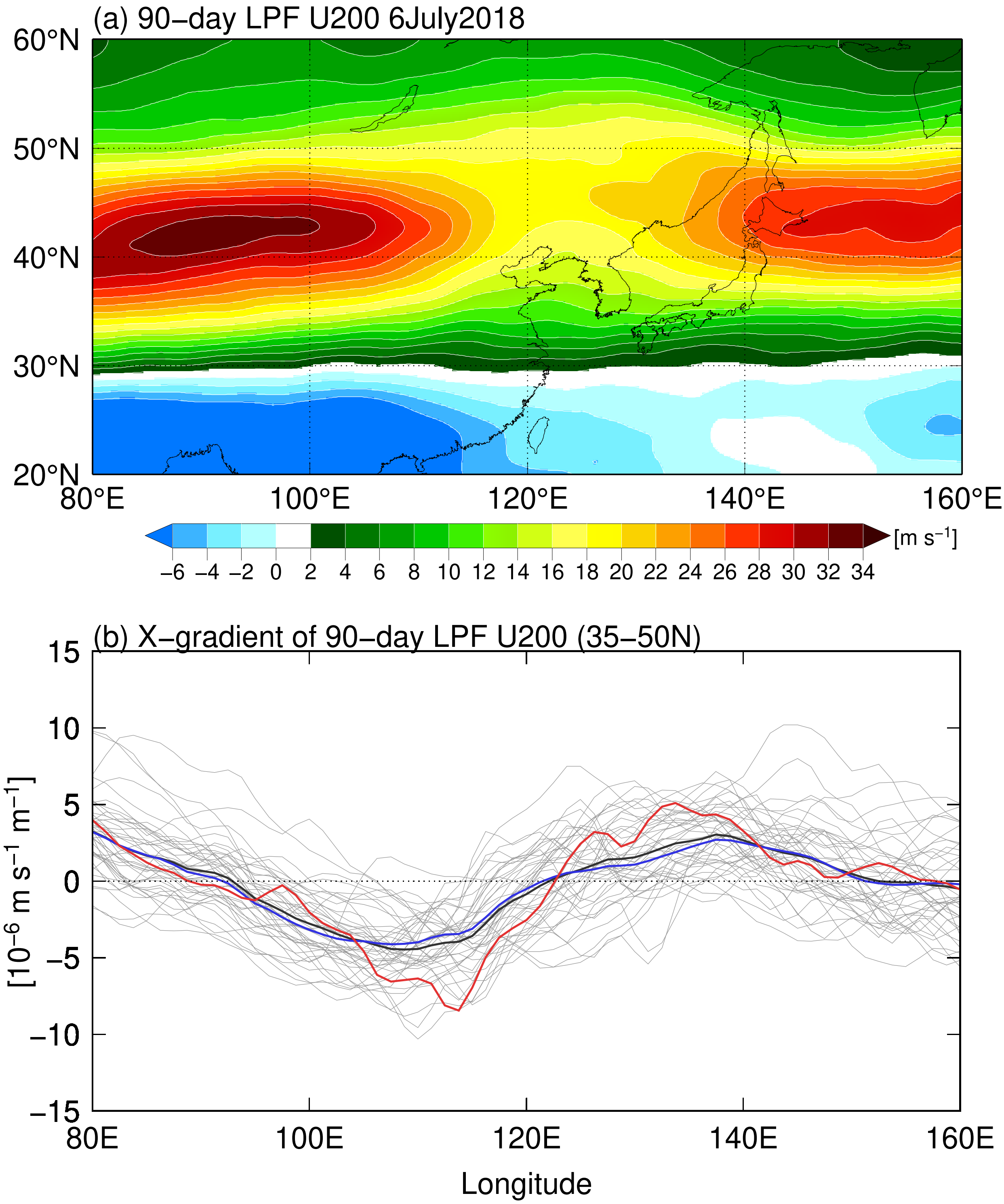

Fig. 15. (a) 90–day LPF 200–hPa zonal wind field on 6 July 2018 and (b) the distribution of the longitudinal gradient of the 90–day LPF 200–hPa zonal wind component (10^{-6} m s^{-1}) averaged over 35–50N for days representing 3–day precipitation peaks during the heavy rainfall events over western Japan that exceed 95th percentile. Gray lines indicate individual cases. The red line indicates for HR18. Blue and black lines represent the average of the heavy rainfall events over western Japan and the climatological mean, respectively.

Table 1. List of top 21 extreme heavy rainfall events in western Japan. Zero value of typhoon flag means that any center of typhoon does not exist within 500 km from the stations in western Japan. Gray shadings indicate the exclusion from composite analysis. The dates represent the central dates for 3-day summation of precipitation.

Rank	Date	3-day precip. [mm]	Typhoon flag
1	06 July 2018	285.9	0
2	05 September 2005	228.5	1
3	28 June 1979	205.9	0
4	03 July 1995	204.2	0
5	18 September 1990	199.7	1
6	27 September 1983	165.3	1
7	18 July 1987	159.1	0
8	03 September 2013	157.8	1
9	02 June 1988	155.3	0
10	29 September 2018	154.7	1
11	09 August 2014	150.9	1
12	03 July 1993	150.5	0
13	13 July 2010	149.1	0
14	03 September 2011	147.5	1
15	20 September 2011	147.5	1
16	13 July 2007	147.3	1
17	19 September 2016	147.2	1
18	02 September 1989	144.9	0
19	09 July 1997	144.9	0
20	20 June 2001	140.0	0
21	24 July 1982	139.2	0